Highly Tunable Junctions and Nonlocal Josephson Effect in Magic Angle Graphene Tunneling Devices

Daniel Rodan-Legrain,[1,*] Yuan Cao,[1,†] Jeong Min Park,[1,‡] Sergio C. de la Barrera,[1] Mallika T. Randeria,[1] Kenji Watanabe,[2] Takashi Taniguchi,[2] and Pablo Jarillo-Herrero[1,§]

[1]*Department of Physics, Massachusetts Institute of Technology, Cambridge, Massachusetts 02139, USA*

[2]*National Institute for Materials Science, Namiki 1-1, Tsukuba, Ibaraki 305-0044, Japan*

(Dated: June 22, 2021)

ABSTRACT

Magic-angle twisted bilayer graphene (MATBG) has recently emerged as a highly tunable two-dimensional (2D) material platform exhibiting a wide range of phases, such as metal, insulator, and superconductor states. Local electrostatic control over these phases may enable the creation of versatile quantum devices that were previously not achievable in other single material platforms. Here, we engineer Josephson junctions and tunneling transistors in MATBG, defined solely by electrostatic gates. Our multi-gated device geometry offers independent control of the weak link, barriers, and tunneling electrodes. These purely 2D MATBG Josephson junctions exhibit nonlocal electrodynamics in a magnetic field, in agreement with the Pearl theory for ultrathin superconductors. Utilizing the intrinsic bandgaps of MATBG, we also demonstrate monolithic edge tunneling spectroscopy within the same MATBG devices and measure the energy spectrum of MATBG in the superconducting phase. Furthermore, by inducing a double barrier geometry, the devices can be operated as a single-electron transistor, exhibiting Coulomb blockade. With versatile functionality encompassed within a single material, these MATBG tunneling devices may find applications in graphene-based tunable superconducting qubits, on-chip superconducting circuits, and electromagnetic sensing.

Tunneling devices are ubiquitous in modern electronics, with applications ranging from tunneling diodes to magnetic tunnel junctions and superconducting Josephson Junctions (JJ). These devices typically involve heterojunctions of different materials to achieve conducting electrodes in series with a weak link or insulating barrier[6,7]. In superconducting circuits, state-of-the-art JJs utilizing oxide tunnel barriers often suffer from disorder and localized states in the noncrystalline barriers[8]. Semiconductor-based JJs necessarily involve heterojunctions, and thus potentially non-ideal interfaces, but offer some advantages for integrated electronics, such as partial tunability of the semiconducting weak link[9,10]. While this offers a number of different operation regimes, the ability to independently tune the electrodes into different phases would enable an exponentially larger number of tunable configurations, qualitatively changing the nature of the device *in situ.* A superconducting junction made of a single clean material, which simultaneously offers a high degree of tunability both in the weak link and in the superconducting electrodes themselves, is therefore highly desirable, but has not been realized to date.

The recent discovery of correlated insulators and superconductivity in MATBG accessible via electrostatic doping[1–4] makes this possible, introducing MATBG as an unexplored material platform for superconducting electronics. In twisted bilayer graphene, a moiré pattern emerges from the coupling between two vertically-stacked graphene lattices with a relative twist angle[11]. Near the first 'magic-angle', a nearly-flat electronic structure[12,13] leads to a large density of states and electron localization in real space around the AA-stacked regions[1,2,14], resulting in strong electronic interactions and emergent many-body correlated states. Using electrostatic gating, a plethora of possible regimes, including p-n junctions, superconducting regions, metallic leads, and insulating islands, among others, become accessible in a single device, making this system attractive both for scientific and technological applications. We exploit this unprecedented tunability to create an all-in-one device that can be used both for superconducting electronics and normal-state operations, bridging the fields of tunable van der Waals materials and superconducting circuits. This could open the door towards fully integrated superconducting electronics, where entire circuits are made out of a single material with local gates and customizable coupling within and between each of the electronic components.

In this Letter, we demonstrate the versatility of multiply-gated MATBG devices. We report on fully tunable lateral JJs, where both the superconducting electrodes and the weak link can be locally controlled. Such JJs additionally provide definitive evidence of superconducting phase coherence in MATBG. Independent control of the weak link is performed via applying a top gate voltage, achieving a junction that can be continuously switched from insulating, metallic, to superconducting regimes, generating a tunable critical supercurrent. In the same multi-gated devices we obtain spectroscopic evidence of the superconducting gap in MATBG by utilizing its intrinsic bandgaps to create lateral tunneling barriers. Finally, inducing barriers on either side of a narrow MATBG strip allows us to transform the device into a single-electron transistor displaying periodic

Coulomb diamonds.

HIGHLY TUNABLE JOSEPHSON JUNCTIONS

To demonstrate these effects, we have measured three superconducting devices labeled A, B, and C. All devices were fabricated using the tear-and-stack dry-transfer technique[1,15,16] (see Methods). Here, we focus on device A with a twist angle $0.95^\circ \pm 0.02^\circ$. The entire device is gated by the back gate, while the top gate is patterned into a narrow strip ($\sim$160 nm) at the center of the device to enable independent control of the region underneath it (Figure 1a). Fig. 1b shows the temperature dependence of the resistance of device A at the optimal doping with $V_{tg} = 0\,\mathrm{V}$, and back gate $V_{bg} = -1.4\,\mathrm{V}$ (corresponding to the blue square in Fig. 1c), displaying a superconducting transition at $T_c \sim 0.85\,\mathrm{K}$, as estimated from 50% of the normal state resistance. The non-linear I-V curves captured near optimal doping (Fig. 1c inset) display zero resistance up to a critical current $I_c \approx 35\,\mathrm{nA}$.

To map out the complex electrostatic response of these devices, we now explore the complete dual-gate parameter space available, which exhibits a number of different insulating, metallic, and superconducting states. Using the back gate and narrow top gate together, we can define three separate regions within the same device with independent phases in series. In each region of the MATBG, when the four-fold valley and spin-degenerate bands are fully filled or fully depleted at densities $n = \pm n_s$, where $n_s = 4/A$ and A is the area of the moiré unit cell, the system behaves as a band insulator[16–18]. In the following, we denote the insulator at $-n_s$ as I, and the insulator at n_s as I'. Correlated insulator states are observed at $n = \pm n_s/2$, and we denote them as C ($-n_s/2$) and C' ($n_s/2$), respectively. Similarly, S and S' denote the superconducting states near $\mp n_s/2$, respectively. Let us also denote D as the charge neutrality (Dirac) point, and n (n') the normal metallic states at fillings $n < -n_s$ ($n > n_s$), when the higher energy dispersive bands become populated by holes (electrons). Metallic states are also observed throughout the flat bands, away from charge neutrality and the correlated fillings, denoted as N. Fig. 1d shows a vertical line cut of the resistance map at $V_{tg} = 0\,\mathrm{V}$. The transition between the different series combinations of the central and outside regions are readily seen from the horizontal and diagonal features of the V_{tg}-V_{bg} resistance map (Fig. 1c). We interpret the diagonal features (dependent on both V_{tg} and V_{bg}) as stemming from the dual-gated region beneath the top gate, and the horizontal features (independent of V_{tg}) as coming from the regions outside the top-gated area. The intersection between a few horizontal (red) and diagonal (green) lines are labeled with black circles in Fig. 1c.

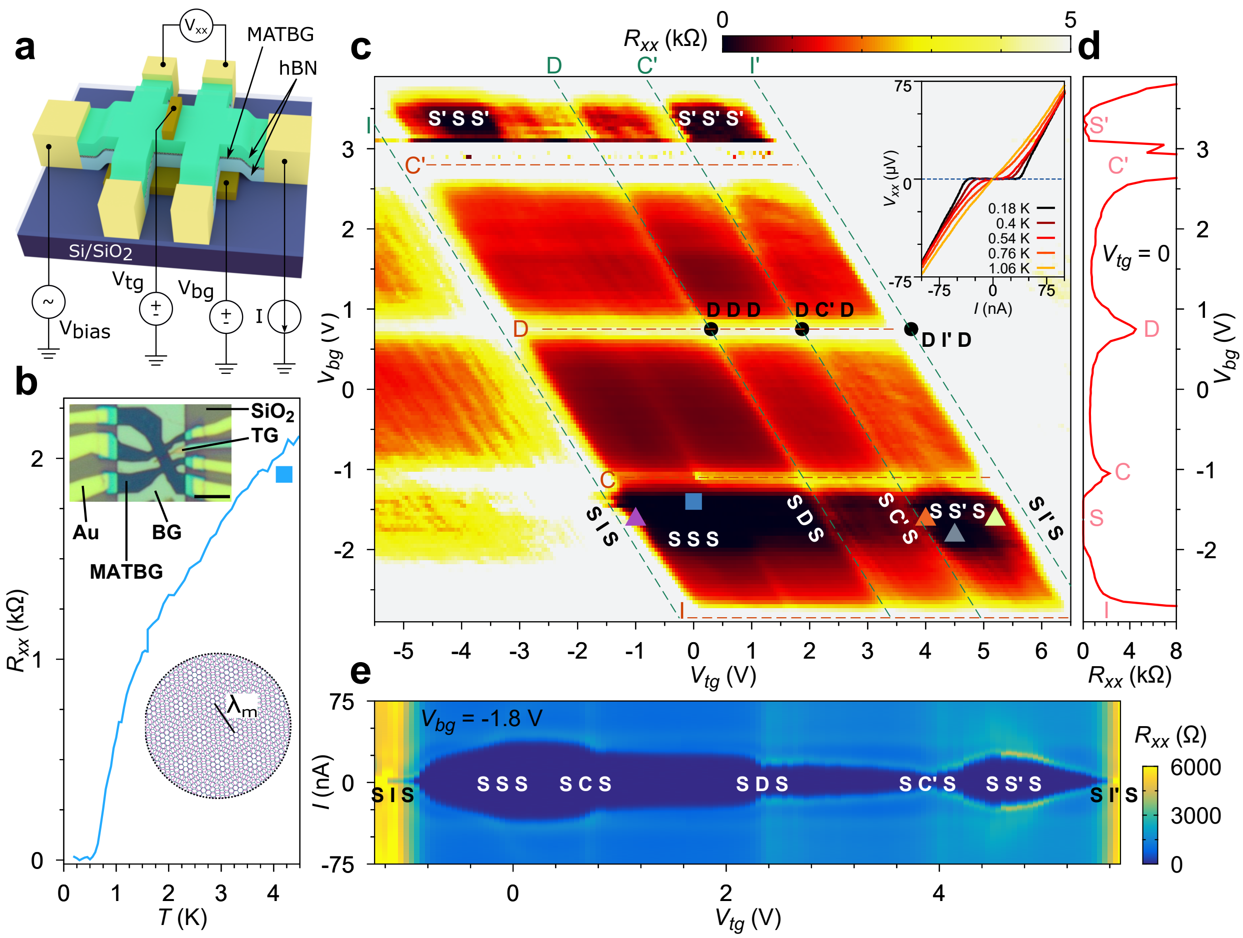

FIG. 1: Device 'A' structure and transport characterization . (a) Schematic illustration: A narrow top gate (∼160 nm wide) controls the electronic state of the region underneath. (b) Resistance vs. temperature curve measured at the blue square in panel (c). Upper left inset: optical image of the final device. A back gate (BG) tunes the electron density in the overlapping region of the MATBG. The narrow top gate (TG) controlling the electronic state of the weak link can be seen at the center of the device. A bias voltage V_{bias} is applied between the drain and source electrodes, and the 4-probe resistance $R_{xx} = V_{xx}/I$ is measured. The scale bar corresponds to 4 µm. Lower right inset: moiré pattern in twisted bilayer graphene. The displayed twist angle is enlarged for clarity with respect to the first magic angle $\theta \approx 1.1°$. The moiré wavelength is given by $\lambda_m = a/[2\sin(\theta/2)]$, where $a = 0.246$ nm is the lattice constant of monolayer graphene, and θ is the twist angle. (c) Resistance as a function of the back gate and the top gate. The dark regions correspond to the superconducting states. Horizontal dashed lines and labels in red denote features induced by the back gate, and diagonal lines and labels in green denote features under the influence of both the top and the back gates. White labels of the form *SXS* or *S'XS'* indicate that at these points the source and drain are in S or S' state while the top-gated region is in the X=I', C', D, S, S', C, or I state. Color-coded triangles indicate the points at which Fraunhofer patterns are taken in Fig. 2. Inset: Current-Voltage curves measured at $V_{bg} = -1.6$ V, $V_{tg} = 0$ V at different temperatures. (d) Line-cut in panel (c) along $V_{tg} = 0$. I = Full filling band insulating state, S = Superconducting, C = Correlated Insulator at Half Filling, D = Dirac (charge neutrality) point. Primes denote positive fillings (i.e., electron doping). (e) Resistance as a function of current bias and top gate voltage, for $V_{bg} = -1.8$ V in the superconducting state.

For example, DDD denotes the coincidence of the Dirac points in all three regions, whereas DC'D occurs when the central region enters the C' correlated insulator state and the outside regions are at charge neutrality, and similarly for other intersections of the dashed lines. More interesting device behavior is obtained by doping away from the horizontal lines in the dual-gate map. For instance, supercurrent through a variable Josephson junction is observed across the device if we use V_{bg} to globally tune the MATBG into S and use V_{tg} to form a weak link with the central region in an insulating state (diagonal labels in Fig. 1c) such as C', or close to the resistance maxima of states I and I' (before the sample becomes fully insulating). Figure 1e illustrates the wide region of supercurrent observed (dark blue), whereas the ability to continuously vary the barrier strength with V_{tg} is indicated by the evolution of the critical current (where the differential resistance becomes finite). We can turn off the supercurrent completely by gating the central region deep into the insulating state (beyond full filling). In this regime the superconducting coherence across the junction is lost, and a dissipative junction is obtained.

NONLOCAL JOSEPHSON EFFECT

Next we address the expected behavior for 2D JJs in the presence of magnetic flux. 2D superconductors screen external magnetic fields in a fundamentally different way from their bulk (3D) counterparts. In ultra-thin superconductors where the film thickness is less than the London penetration depth λ, the characteristic length that governs the spatial magnetic field distribution is given by the Pearl length[5] $\Lambda = 2\lambda^2/d \gg \lambda$, where d is the film thickness. In the case of MATBG, the thickness is less than 1 nm and the Pearl length can reach macroscopic dimensions, exceeding the dimensions of the device itself. Under such conditions, the screening currents cannot effectively expel the external magnetic field (illustrated in Fig. 2a), in striking contrast with bulk samples (Fig. 2b). The origin of this effect can be understood by recognizing that the self-field of the screening current in a thin-film superconductor scales as $\frac{w}{\Lambda}B$, where w is the lateral dimension of the sample and B is the external magnetic field[19]. When $w \ll \Lambda$, the self-field is therefore negligible compared to the external field, allowing finite field penetration.

The distribution of Josephson current and magnetic flux in a JJ is altered in the 2D limit as well. In a bulk JJ, the magnetic field only penetrates a distance $\sim \lambda$ into the superconductor and is therefore mostly confined within the junction barrier. The phase difference across the junction is a simple function that only depends on λ and B. On the other hand, for edge-type Josephson junctions in ultra-thin films, the magnetic field distribution is not confined to the tunneling barrier

(Fig. 2c). An additional distinction between bulk and edge-type 2D JJs is that the Josephson electrodynamics are nonlocal in the 2D case, that is, the magnetic flux in the junction results from a non-negligible superconducting phase gradient in both 2D superconducting regions[6,20–22].

In Fig. 2c-d, we simulate the magnetic field and the screening currents in a bulk JJ and a 2D JJ with similar dimensions as device A, placed in an external magnetic field $\mathbf{B} = B_0\hat{z}$[19,23,24]. From the magnetic field distribution, we can obtain the distribution of the phase difference across the junction which gives rise to the Fraunhofer interference pattern (SI section IX). Our calculated field dependence of the maximum supercurrent in the 2D JJ, in agreement with previous analytical and numerical predictions[19,23–25], differs noticeably from the typical Fraunhofer pattern of bulk junctions in two ways (Fig. 2e). First, the high-field periodicity $\sim 1.8\Phi_0/w^2$ depends solely on the geometry of the sample and is usually much smaller than the bulk periodicity $\Phi_0/w(a+2\lambda)$, where a is the length of the weak link itself. Second, unlike the bulk case, the zeros of $I_c(B)$ for edge-type thin-film junctions are not equidistant at low-fields.

We now present measurements to test these predictions experimentally. Based on the analytical expression $1.8\Phi_0/w^2$, we expect an interference period $\sim$1.7 mT in device A ($w \approx 1.5\,\mu\mathrm{m}$). We first gate the device into the SIS regime, pushing the middle region as far as possible into the insulating region while maintaining superconducting coherence across the junction (Fig. 3a). We observe field-induced oscillations in the critical current with a periodicity of $\sim$1–1.5 mT for the finest oscillations. An approximation of the bulk formula Φ_0/wl using $l \approx a$ gives a periodicity of 8.5 mT, significantly larger than the measured oscillation period. However, our measured periodicity of $\sim$1–1.5 mT is clearly in agreement with the simulations (Fig. 2e) and consistent with the Pearl regime governing the ultrathin superconducting electrodes. This anomalous periodicity is further corroborated by devices B and C (Figs. S5,S7). Critical current oscillations with similar periodicity are also observed close to the SC'S (Fig. 3b) and SI'S (Fig. 3c) configurations. Slight deviations from ideal Fraunhofer behavior and differences between each pattern may be attributed to inhomogeneities and asymmetries across each junction. Josephson oscillations with correlated insulator barriers are weaker in comparison to the SIS and SI'S configurations, possibly due to smaller bandgaps in C, C' compared to I, I', as determined by thermal activation[1]. Overall, a weak link between superconducting regions is achievable in this geometry using different insulating phases. Alternatively, if we bring the weak link into the SS'S regime, the oscillations in the critical current disappear (Fig. 3d). Another piece of evidence for the nonlocal Josephson effect[21] is the resistance as a function of the magnetic field and temperature of the junction close to the SIS regime (Fig. 3f). The oscillation period does not change as the temperature approaches T_c. This is in contrast to the expected behavior in the local regime where, since $\lambda(T)$ diverges as $T \to T_c$, one expects the oscillation period, which is inversely proportional to λ, to be progressively suppressed with temperature[26].

In the SnS regime, we find oscillatory behavior of the critical current with respect to V_{tg} (Fig. 3e). We attribute this to a Fabry-Pérot-like resonance from the interfaces between the dual-gated region and the singly gated regions, which occurs in high-quality devices close to the ballistic transport regime[27,28]. In a JJ, I_c and the normal state resistance R_N typically scale inversely with each other (the Ambegaokar-Baratoff relationship[6]). When the Fabry-Pérot resonance of the electron wave becomes prominent, R_N and I_c are periodically modulated by $\sqrt{n+n_s}$. We observe the resonance only in the SnS regime, likely due to the low effective mass and high mobility in the dispersive band at $n < -n_s$.

TUNNELING SPECTROSCOPY IN THE SUPERCONDUCTING REGIME

We now turn our attention to devices B and C with the structure shown in Fig. 4a. Instead of the narrow top gate in device A, here we pattern two isolated top gates separated by a narrow gap, allowing us to realize a p-n junction. In Fig. 4b, we show the simulated charge carrier density distribution across a gate-defined p-n junction (relative to $-n_s$) in a scenario similar to device B (SI section X). The density evolves continuously and crosses the value $n = -n_s$ at a position between the left gated and right gated regions. Due to quantum capacitance effects in MATBG, a narrow region is kept inside the bandgap at $-n_s$ and acts as a tunneling barrier. If we put one side of the junction in the S state, we then realize an nIS configuration, enabling edge tunneling spectroscopy into the S state, where the tunneling current flows between the 1D edge along the n-I boundary and the 1D edge along the I-S boundary. Using this configuration, in Fig. 4c-f we show tunneling spectra of MATBG in the superconducting regime.

The data show clear spectroscopic evidence of a superconducting gap, including well-defined coherence peaks and a minimum at zero bias. We fit the spectral lineshape to a model for the quasiparticle density of states in an nIS junction to obtain a quantitative measure of the gap. Choosing the simplest such model, that of a conventional isotropic s-wave order parameter[6], we incorporate the effects of thermal and lifetime broadening, and extract a gap of $\Delta_{\mathrm{fit}} = 44\,\mu\mathrm{eV}$ at $T = 95\,\mathrm{mK}$ for device B, and $\Delta_{\mathrm{fit}} = 51\,\mu\mathrm{eV}$ at $T = 100\,\mathrm{mK}$ for device C (see SI section XII). The tunneling conductance minimum and coherence peaks are well captured by this fit, including the absence of a hard gap due to thermal broadening at the lowest experimental temperature. We note

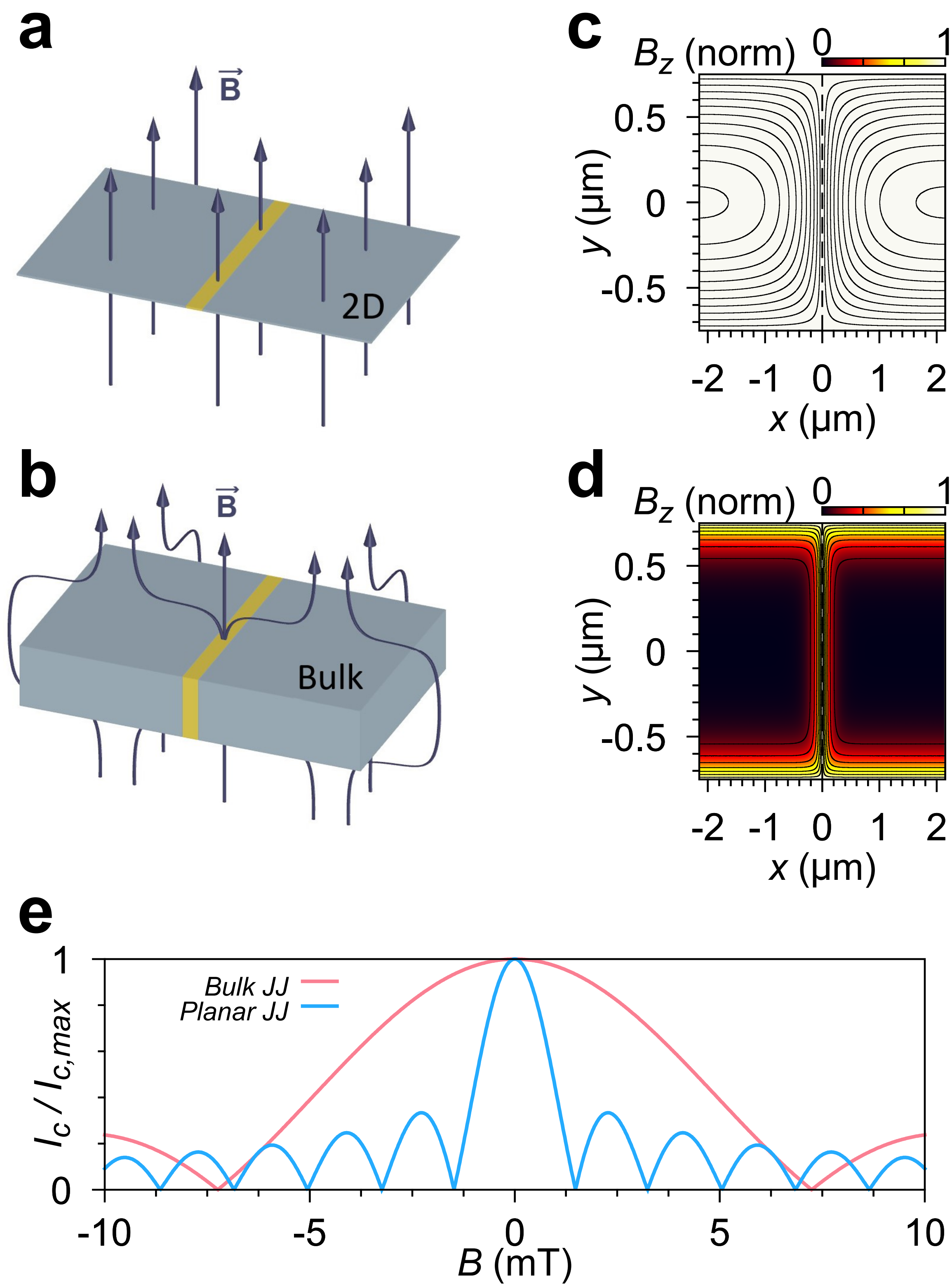

FIG. 2: Comparison of planar 2D and bulk Josephson junctions. (a-b) Schematic representation of (a) a planar 2D Josephson junction and (b) a bulk Josephson junction in an external magnetic field. (c-d) Simulated distribution of the normalized magnetic field B_z in a Josephson junction located at $x = 0$ in the case of (c) planar and (d) bulk superconductor (see SI section IX for details). While in bulk superconductors (d), the magnetic field decays exponentially at the edges within a distance λ, in the 2D case (c), it is essentially unaltered across the entire sample area. The streamlines denote the flow of screening currents in the superconductor. The bulk case assumes a penetration depth of $\lambda = 100\,\mathrm{nm}$. (e) Calculated critical current (normalized) as a function of the magnetic field for bulk and planar Josephson junctions.

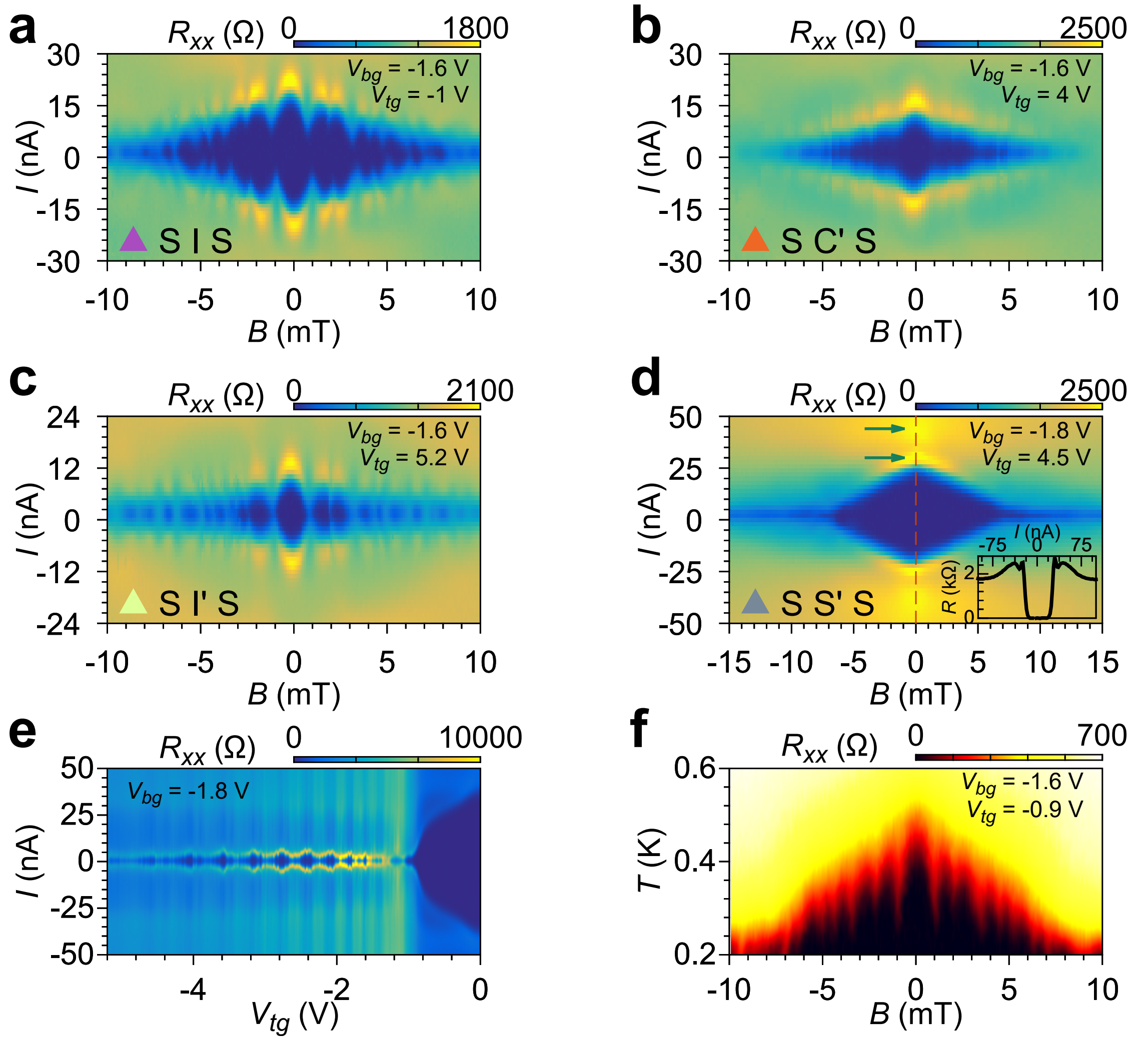

FIG. 3: Nonlocality and tunability of MATBG Josephson junctions. (a-d) Measured Fraunhofer pattern in device A (a) close to SIS regime, (b) SC'S regime, (c) SI'S regime, and (d) SS'S regime. Color-coded triangles correspond to those in Fig. 1c. Inset in (d) shows a linecut across the red dashed line at $B = 0$ T. The two pairs of peaks in the curve correspond to the critical currents of the S and S' states, respectively (green arrows in main panel). (e) Fabry-Pérot-like oscillations in the critical current. (f) Resistance as a function of magnetic field and temperature of the junction close to the SIS regime.

that, microscopically, the density distribution is more intricate than the ideal nIS profile due to the nature of the edge tunneling scheme (Fig. 4b). The energy spectra may include a contribution from proximitized normal regions $\tilde{\mathrm{N}}$ between the superconductor and the insulating state (resulting in an nI$\tilde{\mathrm{N}}$S distribution), in addition to other weaker superconducting states, thus leading to an underestimation of the superconducting gap. Taking the $\Delta_{\mathrm{fit}} = 51\,\mu\mathrm{eV}$ for device C as a lower bound for the superconducting gap at zero temperature ($\Delta_{\mathrm{fit}} \lesssim \Delta_0$), we can estimate an associated transition temperature from the BCS approximation $T_c \gtrsim \Delta_{\mathrm{fit}}/(1.764 k_B) \approx 340\,\mathrm{mK}$. This value is reasonable considering the transition temperature extracted from 50% of the normal-state resistance at a nearby doping value, ∼400 mK (see SI section VIII). However, we emphasize that such a fitting procedure cannot distinguish the symmetry of the superconducting order parameter in our data, as there is significant spectral broadening due to temperature, disorder, and the lateral junction geometry. In fact, we have found equally good quality fits using other non s-wave order parameters. Direct measurements of the pairing symmetry in MATBG remain a fundamental yet unresolved question in the field, and these device structures may be adapted to shed light on this topic.

As the temperature is increased above ∼300 mK (for both devices B and C), the coherence peaks are significantly broadened due to thermal excitations. As the temperature is further increased, the dip at $V_{\rm bias} = 0$ is suppressed and eventually disappears, indicating that the system is no longer superconducting. Similarly, by applying a perpendicular magnetic field at base temperature, the coherence peaks are also suppressed at $B \approx 50\,$mT for device B ($B \approx 100\,$mT for device C), comparable to the upper critical field observed in transport in magic-angle devices with similar T_c[2]. The closing of the gap and suppression of the coherence peaks with temperature and magnetic field further support a superconducting origin for the observed gap. A portion of the tunneling minimum at zero bias persists to much larger magnetic fields, however, a similar tunneling minimum is observed above the critical field for a wide range of densities outside of the superconducting dome, without associated coherence peaks at zero field (Fig. S9), and thus arises from a distinct mechanism. Such a suppression in the tunneling spectra may be related to the Efros-Shklovskii-type Coulomb gap that arises at the Fermi level due to localization in disordered semiconducting thin films[29,30], or alternatively, it may result from electronic interactions during the tunneling process[31–33]. Although we consistently observe a suppression in the tunneling conductance at zero bias for all three measured devices, further detailed studies are required to determine the precise origin of this spectral feature.

SINGLE-ELECTRON TRANSISTOR REGIME

Further exploiting the flexibility of the split-gate geometry, we can create a single-electron transistor (SET) within the same multipurpose devices. To achieve this, we tune the left and right top gates to bring the two sides of the device into metallic states with densities $n < -n_s$. The central narrow region, being singly gated, is brought into the density range $-n_s < n < -n_s/2$. With similar arguments as those mentioned above, two insulating plateaus with $n = -n_s$ form

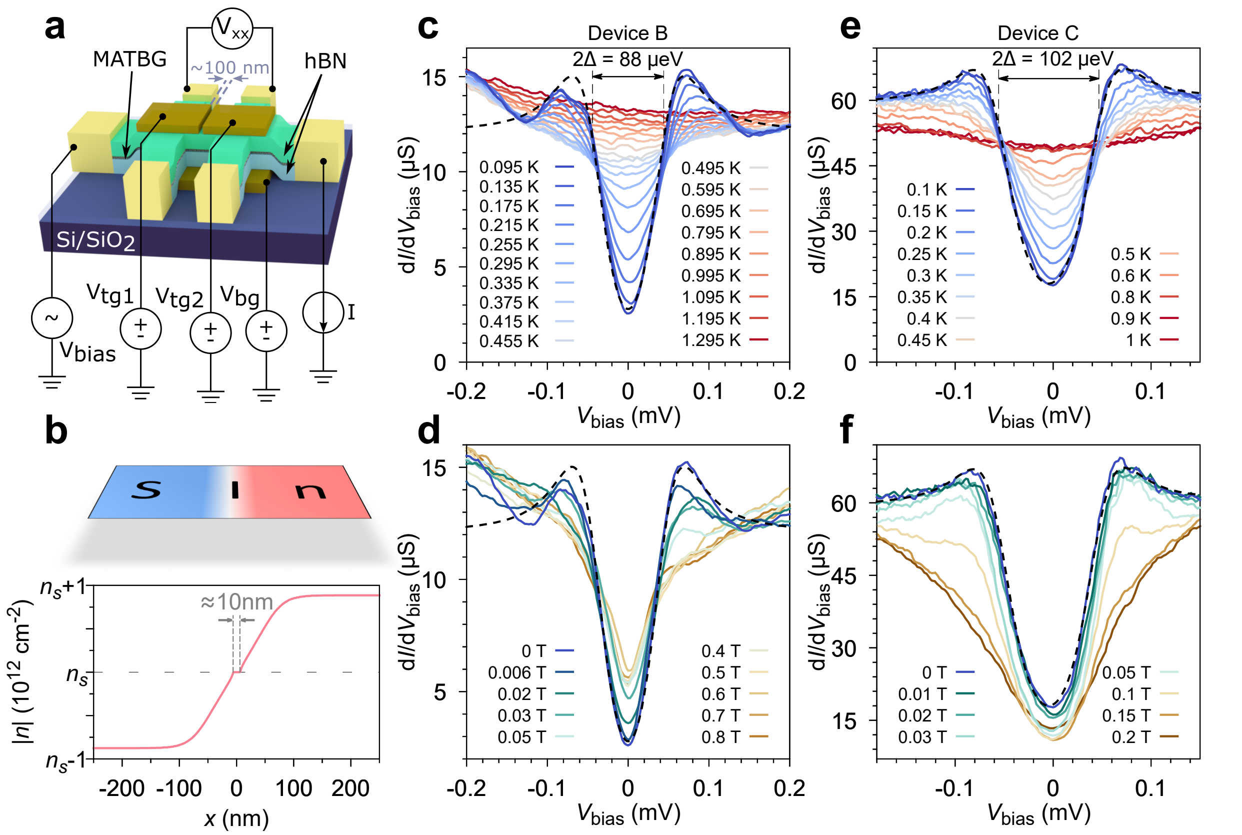

FIG. 4: Edge tunneling spectroscopy of the superconducting gap in MATBG. (a) Structure of devices B and C with two top gates separated by a narrow gap. (b) Numerical calculated charge carrier density distribution in the p-n junction regime performed for device B (device C analogous). The left half is brought into the superconducting state S at $n \approx -0.6n_s$, while the right half is brought into a normal metallic regime with density $n \approx -1.4n_s$ (all densities are for hole doping and thus are all negative). In the central region of the device, the density passes through the band insulator I ($n = -n_s$), thus creating a tunneling barrier. (c) Raw tunneling spectra as a function of temperature, from 0.095 K to 1.295 K for device B. The black dashed line is a theoretical fit to the quasiparticle density of states (SI section XII), yielding an extracted gap $\Delta_{\text{fit}} = 44\,\mu\text{eV}$ (with negligible broadening). (d) Magnetic field dependence of the edge tunneling spectra, from 0 T to 0.8 T for device B. (e) Similarly, tunneling spectra as a function of temperature and (f) perpendicular magnetic field for device C, with the left half of the device in the superconducting state S at $n \approx -0.775n_s$, and the right half at a density $n \approx -1.2n_s$. The dashed line is the theoretical fit giving an extracted corresponding gap $\Delta_{\text{fit}} = 51\,\mu\text{eV}$ (with Dynes broadening 15 μeV).

around the central region of the sample, resulting in an isolated island in the middle. Fig. 5a illustrates such an nINIn configuration, as seen from above, and the calculated charge carrier density distribution. At low temperatures ($k_B T \ll e^2/C_\Sigma$, where C_Σ is the total capacitance of the island) and with large tunneling resistance ($R_{\text{tunnel}} \gg h/e^2$), electron tunneling is allowed only if there are available discrete energy levels between the Fermi energies of the source and the drain (Fig. 5b), whereas the Coulomb blockade effect prohibits tunneling otherwise (Fig. 5c)[6,34].

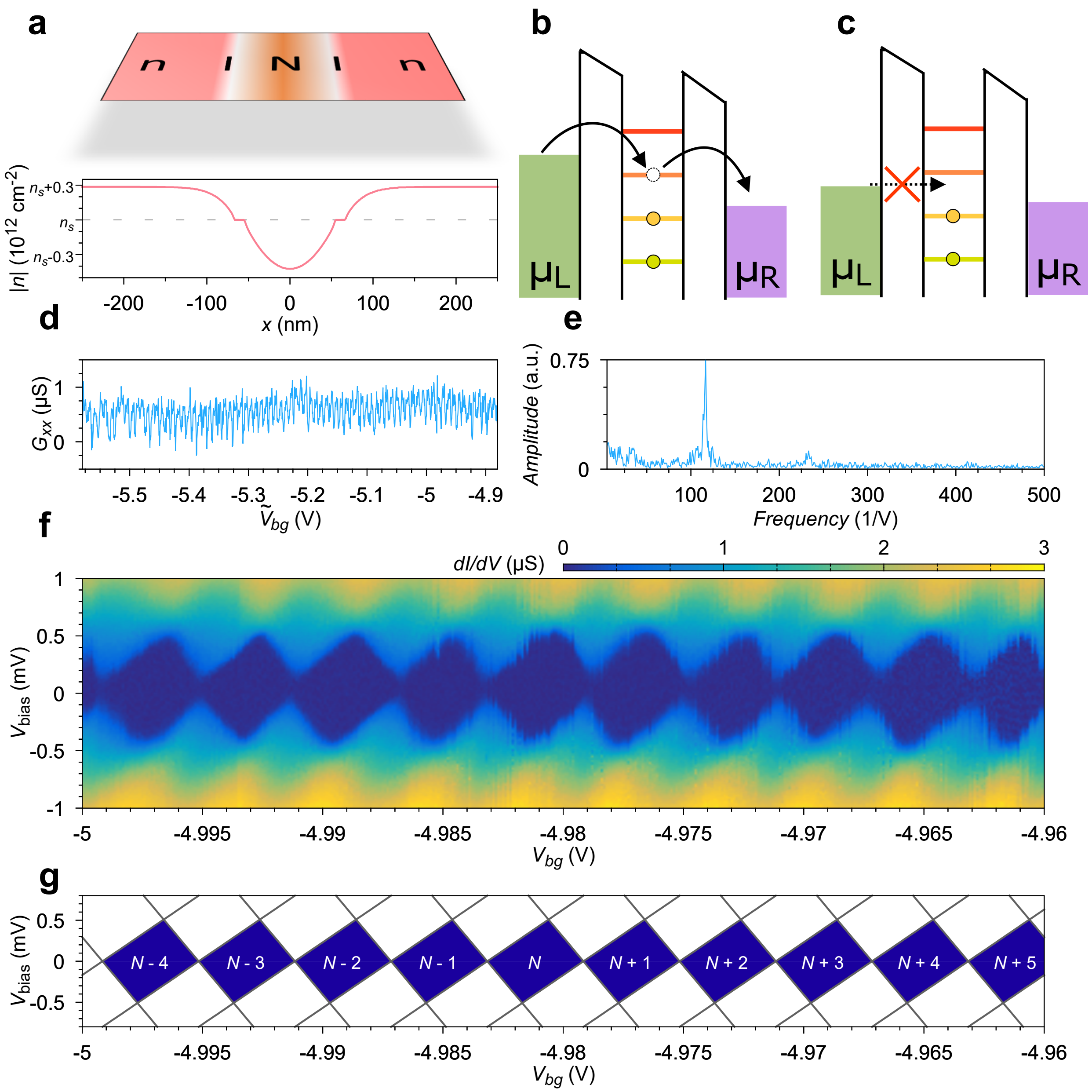

FIG. 5: Electrostatically defined single-electron transistor and Coulomb blockade in MATBG. (a) Gating scheme of the device and simulation of the charge density across the sample. Two effective insulating barriers emerge, and the central island can be operated as a single-electron transistor. (b-c) Schematic space-energy diagram of a single-electron transistor in the (b) conducting and (c) Coulomb blockade regimes. μ_L and μ_R are the chemical potentials of the source and drain electrodes, respectively. (d) Conductance versus back gate voltage V_{bg}, while the two top gates keep the densities on the source and drain at $n \approx -1.1n_s$. (e) Fourier transform of the two-probe tunneling current, showing a single peak at $116\,\mathrm{V}^{-1}$. (f) Differential conductance as a function of back gate voltage and source-drain bias voltage. Pronounced Coulomb diamonds, corresponding to the absence of tunneling current, are observed. In this scan, only the back gate is swept while both top gates are fixed. (g) Schematic of the Coulomb diamonds (see main text). N denotes the number of electrons in the central island. The mismatch of the periodicities in panels (d-e) and panels (f-g) is attributed to cross-coupling of the top gates and is discussed in SI section VII (we have added a tilde in the x-axis label of panel (d) to avoid possible confusion). All the data in this figure correspond to device B.

In Fig. 5d, we measure the tunneling conductance of the gate-defined single-electron transistor as the back gate voltage is varied, keeping the source and drain densities fixed. The signal displays fine, reproducible oscillations as a function of the back gate voltage. A Fourier transform of the measured tunneling current reveals a single periodicity (Fig. 5e). Figure 5f shows the differential conductance in a narrower range of back gate voltages, as a function of the source-drain bias voltage. We observe well-developed Coulomb diamonds with zero conductance in the blockaded regime. These observations are in agreement with a single-electron transistor with capacitances $C_g = 40\,\mathrm{aF}$, $C_1 \approx C_2 = 110\,\mathrm{aF}$, $C_\Sigma = 310\,\mathrm{aF}$ (see SI section VII for definitions), as shown in Fig. 5g. Thus we find that the band insulator in MATBG provides a suitable barrier for SET physics in graphene with appropriate local gating, adding to the broad tunability of these MATBG devices.

CONCLUSIONS

The unprecedented tunability of MATBG together with local electrostatic gating in this work enables complete control of the weak link and junction electrodes, independently. With this versatile platform, we demonstrate multiple Josephson junctions with differing barrier strength and character, edge-tunneling spectroscopy of the superconducting state, and robust SET physics in a double-barrier configuration. While multiple devices are presented here, critically, all three aforementioned experiments are achievable in a single device geometry. Gate-defined tunnel junctions present a significant advance toward probing the superconducting order parameter in MATBG, and will inspire further advances for exploring physics within the expanding class of moiré systems. Furthermore, these multipurpose devices establish a clear path toward gate-defined circuits with MATBG in future 2D integrated electronics, with potential applications in low-temperature circuits, quantum computing, and electromagnetic sensing.

Note: during the preparation of this manuscript, we became aware of related work[35]

---

[1] Cao, Y. *et al.* Correlated insulator behaviour at half-filling in magic-angle graphene superlattices. *Nature* **556**, 80–84 (2018).

[2] Cao, Y. *et al.* Unconventional superconductivity in magic-angle graphene superlattices. *Nature* **556**, 43–50 (2018).

[3] Yankowitz, M. *et al.* Tuning superconductivity in twisted bilayer graphene. *Science* **363**, 1059–1064 (2019).

[4] Lu, X. *et al.* Superconductors, orbital magnets and correlated states in magic-angle bilayer graphene. *Nature* **574**, 653–657 (2019).

[5] Pearl, J. Current distribution in superconducting films carrying quantized fluxoids. *Applied Physics Letters* **5**, 65–66 (1964).

[6] Tinkham, M. *Introduction to Superconductivity* (Dover Publications, 2004), 2nd edn.

[7] Likharev, K. K. Superconducting weak links. *Rev. Mod. Phys.* **51**, 101–159 (1979).

[8] Oliver, W. D. & Welander, P. B. Materials in superconducting quantum bits. *MRS Bulletin* **38**, 816–825 (2013).

[9] Larsen, T. *et al.* Semiconductor-Nanowire-Based Superconducting Qubit. *Physical Review Letters* **115**, 127001 (2015).

[10] Wang, J. I.-J. *et al.* Coherent control of a hybrid superconducting circuit made with graphene-based van der Waals heterostructures. *Nature Nanotechnology* **14**, 120–125 (2019).

[11] Li, G. *et al.* Observation of Van Hove singularities in twisted graphene layers. *Nature Physics* **6**, 109–113 (2010).

[12] Suárez Morell, E., Correa, J. D., Vargas, P., Pacheco, M. & Barticevic, Z. Flat bands in slightly twisted bilayer graphene: Tight-binding calculations. *Physical Review B* **82**, 121407 (2010).

[13] Bistritzer, R. & MacDonald, A. H. Moiré bands in twisted double-layer graphene. *Proceedings of the National Academy of Sciences* **108**, 12233–12237 (2011).

[14] Lopes dos Santos, J. M. B., Peres, N. M. R. & Castro Neto, A. H. Continuum model of the twisted graphene bilayer. *Physical Review B* **86**, 155449 (2012).

[15] Kim, K. *et al.* van der Waals Heterostructures with High Accuracy Rotational Alignment. *Nano Letters* **16**, 1989–1995 (2016).

[16] Cao, Y. *et al.* Superlattice-Induced Insulating States and Valley-Protected Orbits in Twisted Bilayer Graphene. *Physical Review Letters* **117**, 116804 (2016).

[17] Kim, K. *et al.* Tunable moiré bands and strong correlations in small-twist-angle bilayer graphene. *Proceedings of the National Academy of Sciences* **114**, 3364–3369 (2017).

[18] Nam, N. N. T. & Koshino, M. Lattice relaxation and energy band modulation in twisted bilayer graphene. *Physical Review B* **96**, 075311 (2017).

[19] Moshe, M., Kogan, V. G. & Mints, R. G. Edge-type Josephson junctions in narrow thin-film strips. *Physical Review B* **78**, 020510 (2008).

[20] Ivanchenko, Y. M. & Soboleva, T. K. Nonlocal interaction in Josephson junctions. *Physics Letters A* **147**, 65–69 (1990).

[21] Boris, A. A. *et al.* Evidence for Nonlocal Electrodynamics in Planar Josephson Junctions. *Physical Review Letters* **111**, 117002 (2013).

[22] Abdumalikov, A. A., Alfimov, G. L. & Malishevskii, A. S. Nonlocal electrodynamics of Josephson vortices in superconducting circuits. *Superconductor Science and Technology* **22**, 023001 (2009).

[23] Clem, J. R. Josephson junctions in thin and narrow rectangular superconducting strips. *Physical*

Review B **81**, 144515 (2010).

[24] Kogan, V. G., Dobrovitski, V. V., Clem, J. R., Mawatari, Y. & Mints, R. G. Josephson junction in a thin film. *Physical Review B* **63**, 144501 (2001).

[25] Rosenthal, P. A., Beasley, M. R., Char, K., Colclough, M. S. & Zaharchuk, G. Flux focusing effects in planar thin-film grain-boundary Josephson junctions. *Applied Physics Letters* **59**, 3482–3484 (1991).

[26] Nagata, S., Yang, H. C. & Finnemore, D. K. Oscillations in the temperature dependence of Josephson supercurrents in SNS junctions. *Physical Review B* **25**, 6012–6014 (1982).

[27] Calado, V. E. *et al.* Ballistic Josephson junctions in edge-contacted graphene. *Nature Nanotechnology* **10**, 761–764 (2015).

[28] Ben Shalom, M. *et al.* Quantum oscillations of the critical current and high-field superconducting proximity in ballistic graphene. *Nature Physics* **12**, 318–322 (2016).

[29] Efros, A. L. & Shklovskii, B. I. Coulomb gap and low temperature conductivity of disordered systems. *Journal of Physics C: Solid State Physics* **8**, L49–L51 (1975).

[30] Lee, M., Massey, J. G., Nguyen, V. L. & Shklovskii, B. I. Coulomb gap in a doped semiconductor near the metal-insulator transition: Tunneling experiment and scaling ansatz. *Physical Review B* **60**, 1582–1591 (1999).

[31] Altshuler, B. L. & Aronov, A. G. Zero bias anomaly in tunnel resistance and electron—electron interaction. *Solid State Communications* **88**, 1033–1035 (1993).

[32] Gershenzon, M. E., Gubankov, V. N. & Falei, M. I. Tunnel spectroscopy of the electron-electron interaction in disordered aluminum films. *Sov. Phys. JETP* **63**, 6 (1986).

[33] Kotel'nikov, I. N., Dizhur, S. E., Morozova, E. N., Devyatov, E. V. & Dolgopolov, V. T. Zero-bias tunneling anomaly in a two-dimensional electron system with disorder. *JETP Letters* **96**, 577–581 (2013).

[34] Ihn, T. *et al.* Graphene single-electron transistors. *Materials Today* **13**, 44–50 (2010).

[35] de Vries, F. K. *et al.* Gate-Defined Josephson Junctions in Magic-Angle Twisted Bilayer Graphene. *arXiv:2011.00011 [cond-mat]* (2020). arXiv:2011.00011.

ACKNOWLEDGEMENTS

We acknowledge helpful discussions with Leonid Levitov, Zhiyu Dong, William D. Oliver, Joel I-Jan Wang, M. A. Mueed and Brian Skinner. This work has been supported by the National Science Foundation through grant DMR-1809802 and by the STC Center for Integrated Quantum Materials (NSF Grant No. DMR-1231319), for partial device fabrication, transport measurements, and data analysis (Y.C., D.R-L.,S.C.B.). Help with transport measurements and data analysis were supported by the US Department of Energy (DOE), Office of Basic Energy Sciences (BES), Division of Materials Sciences and Engineering under Award DE-SC0001819 (J.M.P.). Partial support for conceptual development and device technology was provided by the US Army Research Office grant no. W911NF-17-S-0001 (D.R-L). D.R-L. acknowledges earlier support from Fundació Bancaria "la Caixa" (LCF/BQ/AN15/10380011). P.J-H acknowledges support from the Gordon and Betty Moore Foundation's EPiQS Initiative through Grant GBMF9643 and general support by the Fundación Ramon Areces. The development of new nanofabrication and characterization techniques enabling this work has been supported by the US DOE Office of Science, BES, under award DE-SC0019300. M.T.R. acknowledges support from the MIT Pappalardo Fellowship. K.W. and T.T. acknowledge support from the Elemental Strategy Initiative conducted by the MEXT, Japan, Grant Number JPMXP0112101001, JSPS KAKENHI Grant Numbers JP20H00354 and the CREST(JPMJCR15F3), JST. This work made use of the Materials Research Science and Engineering Center Shared Experimental Facilities supported by the National Science Foundation (DMR-0819762) and of Harvard's Center for Nanoscale Systems, supported by the NSF (ECS-0335765).

AUTHOR CONTRIBUTIONS

D. R.-L., Y.C. and J.M.P. fabricated samples and performed transport measurements. D. R.-L., Y.C., J.M.P., S.D.L.B., M.T.R and P.J-H. performed data analysis and discussed the results. Y.C. performed the numerical simulations. P.J-H supervised the project. K.W. and T.T. provided h-BN samples. D.R.-L., Y.C., J.M.P, S.D.L.B., M.T.R. and P.J.-H. co-wrote the manuscript with input from all co-authors.

AUTHOR INFORMATION

The authors declare no competing financial interest.

METHODS

Fabrication and measurements

Our devices comprise a 4-layer van der Waals heterostructure placed in between two metallic gates, as illustrated in Fig. 1a and Fig. 4a of the main text. All devices were fabricated using the tear-and-stack dry-transfer technique[1,15,16], which enables us to achieve high-quality devices with clean interfaces and twist angles close to the first magic angle, $\theta \approx 1.1^{\circ}$. From bottom to top, they all have a gold/palladium (60/40) back gate, a bottom hexagonal boron nitride substrate (hBN), MATBG, a top hBN, and a gold top gate. Device A has a narrow top gate, while devices B and C have two top gates separated by a narrow gap. All the two-dimensional materials are obtained via mechanical exfoliation on a SiO_2/Si chip, and high-quality flakes are carefully selected using optical microscopy and atomic force microscopy.

The van der Waals heterostructure is assembled via a modified polymer-based dry pick up and transfer technique. A poly(bisphenol A carbonate) (PC) thin film (Fluka Analytical, part number 181641) covering a polydimethylsiloxane (PDMS) 2 mm x 2 mm piece, lying on a glass slide and mounted on a custom-made micro-positioning stage, is used to successively pick up the topmost hBN and the graphene sheets with high success rates. The hBN flake is picked up by heating the substrate in contact with PC up to 110°C. Graphene is torn in half at room temperature by the van der Waals forces between the hBN and the region of the graphene flake in contact with the hBN. The remaining half of the graphene is rotated to angle close to 1.1° and then picked up. The full stack is then released onto the previously prepared bottom hBN on a metallic back gate, by melting the PC at 170°C. Finally, the PC film is dissolved in a chloroform bath.

The first step of fabrication is an etching step in order to minimize relaxation of the graphene layers during subsequent steps. The geometry of this etch mask is larger than the actual final device, but must lie (at least partially) on the inner part of the two graphene layers, while leaving a path for the top gate.

Then the device is again patterned by electron-beam lithography to define the edge contacts. Following another reactive ion etching, the device is mounted on a tilted rotating stage and edge-contacted by thermally evaporated chromium/gold[36]. Liftoff is performed in acetone at room temperature. To define the narrow top gate (device A), or two top gates (devices B and C), one more electron beam lithography, thermal evaporation, and liftoff steps are needed. Finally, the device geometry is defined via reactive ion etching, followed by an oxygen plasma etching to remove possible graphene or graphite residues shorting the contacts. We illustrate in Fig. S1 the fabrication sequence for device A as a paradigmatic example of one of our top gated devices.

After mounting the finalized device on a chip carrier and wire-bonding it, the device is measured in a Triple-Axis Dilution Refrigerator with base temperature around 70 mK. All data were acquired using standard low-frequency lock-in techniques. Both the current flowing through the sample and the four-probe voltages are amplified during measurements using a current pre-amplifier and a voltage pre-amplifier, respectively, and then measured using different SR-830 lock-in amplifiers that are all synchronized to a frequency of 1 Hz $\sim$ 20 Hz. The sample resistance is obtained by dividing the four-probe voltage V_{xx} by the current flowing through the sample I (excitation current $I_{ac} \approx 1\,\mathrm{nA}$). Around 50% of the measured devices fabricated following this procedure displayed correlated insulating states at half-filling and superconductivity. For the other devices, the twist angle typically deviated from the *magic-angle* ($\theta \approx 1.1^\circ$), and displayed transport signatures characteristic of lower or larger twist angle devices.

DATA AVAILABILITY

Source data are provided with this paper. The data that support the findings of this study are available from the corresponding author upon reasonable request.

[36] Wang, L. *et al.* One-Dimensional Electrical Contact to a Two-Dimensional Material. *Science* **342**, 614–617 (2013).

Supplementary Information for 'Highly Tunable Junctions and Nonlocal Josephson Effect in Magic Angle Graphene Tunneling Devices'

CONTENTS

I. FABRICATION AND MEASUREMENTS

Our devices comprise a 4-layer van der Waals heterostructure placed in between two metallic gates, as illustrated in Fig. 1a and Fig. 4a of the main text. From bottom to top, they all have a gold/palladium (60/40) back gate, a bottom hexagonal boron nitride substrate (hBN), MATBG, a top hBN, and a gold top gate. Device A: bottom hBN 28 nm, top hBN 25 nm. Device B: bottom hBN 55 nm, top hBN 26 nm. Device C: bottom hBN 50 nm, top hBN 50 nm. Device A has a narrow top gate, while devices B and C have two top gates separated by a narrow gap. All the two-dimensional materials are obtained via mechanical exfoliation on a SiO_2/Si chip, and high-quality flakes are carefully selected using optical microscopy and atomic force microscopy. First, $\sim$30 nm-thick back gates are patterned with e-beam lithography and thermal evaporation of Cr and Pd/Au. Heat annealing in forming gas (H_2/Ar) is employed to clean the gates. All gates are first inspected optically and then via AFM to confirm their thickness, guarantee they do not show traces of organic residues, and check they are flat without visible inhomogeneities. After that, a bottom hBN flake is placed on top of each local metallic gate, and heat annealed again to remove possible residues from the removal of polymer. An AFM "tip cleaning" [1, 2] can be optionally performed to "broom" the remaining polymer residues off the hBN.

The van der Waals heterostructure is assembled via a modified polymer-based dry pick up and transfer technique. A poly(bisphenol A carbonate) (PC) thin film (Fluka Analytical, part number 181641) covering a polydimethylsiloxane (PDMS) 2 mm x 2 mm piece, lying on a glass slide and mounted on a custom-made micro-positioning stage, is used to successively pick up the topmost hBN and the graphene sheets with high success rates. The hBN flake is picked up by heating the substrate in contact with PC up to 110°C. Graphene is torn in half at room temperature by the van der Waals forces between the hBN and the region of the graphene flake in contact with the hBN. The remaining half of the graphene is rotated to angle close to 1.1° and then picked up. The full stack is then released onto the previously prepared bottom hBN on a metallic back gate, by melting the PC at 170°C. Finally, the PC film is dissolved in a chloroform bath for 5 minutes.

The device geometry is designed using a CAD software, based on the optical and AFM micrographs of the stack (Fig. S1c), keeping only the cleanest and bubble-free parts of the twisted bilayer region. The first step of fabrication is an etching step in order to minimize relaxation of the graphene layers during subsequent steps. The etch mask is electron-beam lithographically defined via Poly(methyl methacrylate) (PMMA 950A5 from Microchem). The geometry of this etch mask is larger than the actual final device, but must lie (at least partially) on the inner part of the two graphene layers, while leaving a path for the top gate.

Then the device is again patterned by electron-beam lithography (double layer resist PMMA 495A5/ PMMA 950A2) to define the edge contacts. Following another reactive ion etching, the device is mounted on a tilted rotating stage and edge-contacted by thermally evaporated chromium/gold (2 nm and around 65 nm∼90 nm, respectively)[3]. Liftoff is performed in acetone for several hours at room temperature (Fig. S1e). To define the narrow top gate (device A) (∼160 nm wide and 25 nm thick), or two top gates (devices B and C), one more electron beam lithography, thermal evaporation, and liftoff steps are needed (Fig. S1f). Finally, the device geometry is defined via reactive ion etching with PMMA etch mask similar to the one described above, followed by an oxygen plasma etching to remove possible graphene or graphite residues shorting the contacts. We illustrate in Fig. S1 the fabrication sequence for device A as a paradigmatic example of one of our top gated devices.

After mounting the finalized device on a chip carrier and wire-bonding it, the device is measured in a Triple-Axis Dilution Refrigerator with base temperature around 70 mK. All data were acquired using standard low-frequency lock-in techniques. Both the current flowing through the sample and the four-probe voltages are amplified during measurements using a current pre-amplifier and a voltage pre-amplifier, respectively, and then measured using different SR-830 lock-in amplifiers that are all synchronized to a frequency of 1 Hz $\sim$ 20 Hz. The sample resistance is obtained by dividing the four-probe voltage V_{xx} by the current flowing through the sample I (excitation current $I_{ac} \approx 1$ nA). Around 50% of the measured devices fabricated following this procedure displayed correlated insulating states at half-filling and superconductivity. For the other devices, the twist angle typically deviated from the *magic-angle* ($\theta \approx 1.1°$), and displayed transport signatures characteristic of lower or larger twist angle devices.

II. LANDAU FAN DIAGRAMS

The magnetotransport data allow us to determine the twist angle of devices A, B, and C, as shown in Fig. S2. The details of the twist angle extraction can be found in our previous works [4–7].

The errors in the angle can be estimated by visually inspecting how well the Landau levels at the Dirac point, $\pm n_s/2$, and $\pm n_s$ fit to the expected Landau fans of a given twist angle. Device A has an estimated twist angle of 0.95° ±0.02, device B has a twist angle 1.2° ±0.05, and device C has a twist angle 0.98° ±0.02.

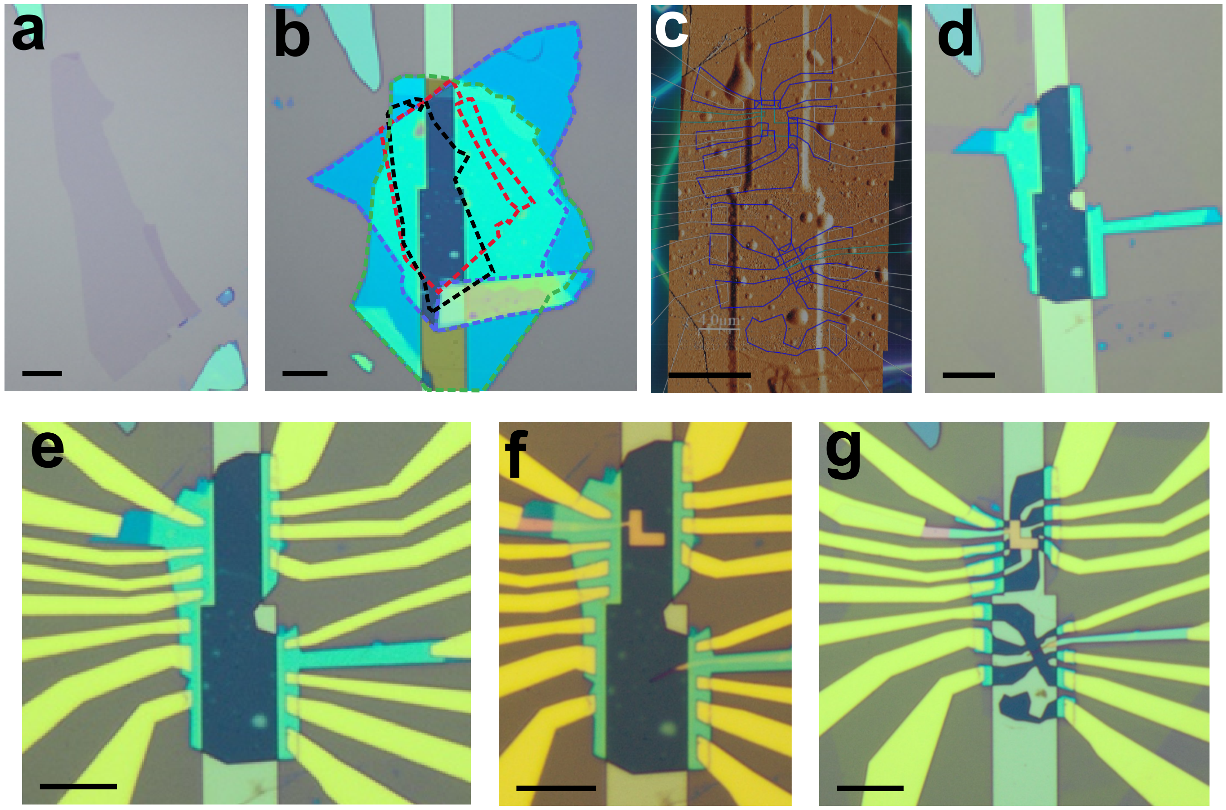

Figure S1. **Fabrication steps of device A**. (a) Optical image of the graphene flake. (b) Resulting stack (blue line indicates the top hBN, green line the bottom hBN, red line the original graphene (but after tearing apart) and black line the second piece of graphene). (c) Design of the stack, based on optical images and AFM amplitude images. (d) Stack after the first broad etching. (e) Optical image after evaporation of the contacts. (f) Optical micrograph after evaporation of the top gate. The finalized image is shown in panel (g). Device A is the lower hall-bar device. The upper device has an L-shaped top gate (not narrow, nor with a gap), and will be reported elsewhere. All scale bars are 8 microns.

III. ADDITIONAL FRAUNHOFER PATTERNS FOR DEVICE A

Figure S3a shows the magnetic field dependence of a horizontal line cut in Fig. 1c of the main text for $V_{bg} = -1.6\,\mathrm{V}$, which gates the source/drain regions into the superconducting state. The vertical red lines label the electronic state of the region under the narrow top gate. By fixing the density at one of those top gates or close-by values, and the back gate such that the rest of the junction is in the superconducting state, our devices can realize a tunable Josephson junction. Figure S3b displays the resistance as a function of top gate and current bias for the back gate in the superconducting state.

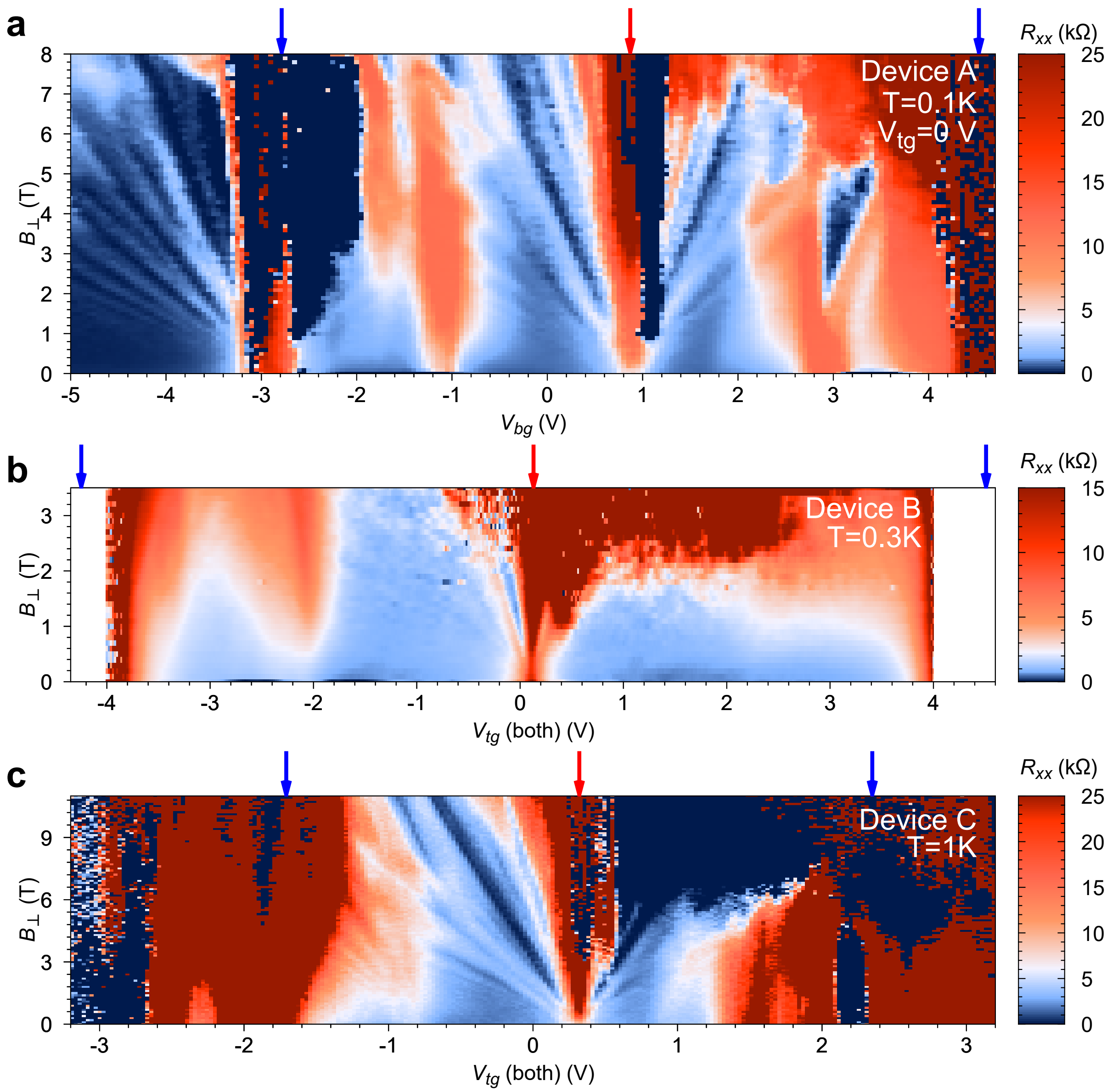

Figure S2. **Landau fan diagrams of devices A, B and C.** (a) Resistance vs. back gate voltage and perpendicular magnetic field with no top gate voltage applied, at base temperature for device A. (b) Resistance vs. top gates voltages (both connected together) and perpendicular magnetic field at 0.3 K, for device B. The back gate voltage is swept simultaneously to the top gates from −4 V to 5 V for each line. (c) Resistance vs. top gates voltages (both connected together) for device C, with top gates both swept from −3.2 V to 3.2 V and simultaneously back gate swept from −8.8 V to 8.1 V at 1 K. Red arrows denote the position of the charge neutrality point for each device, and the blue arrows denote the extracted position of $n = \pm n_s$.

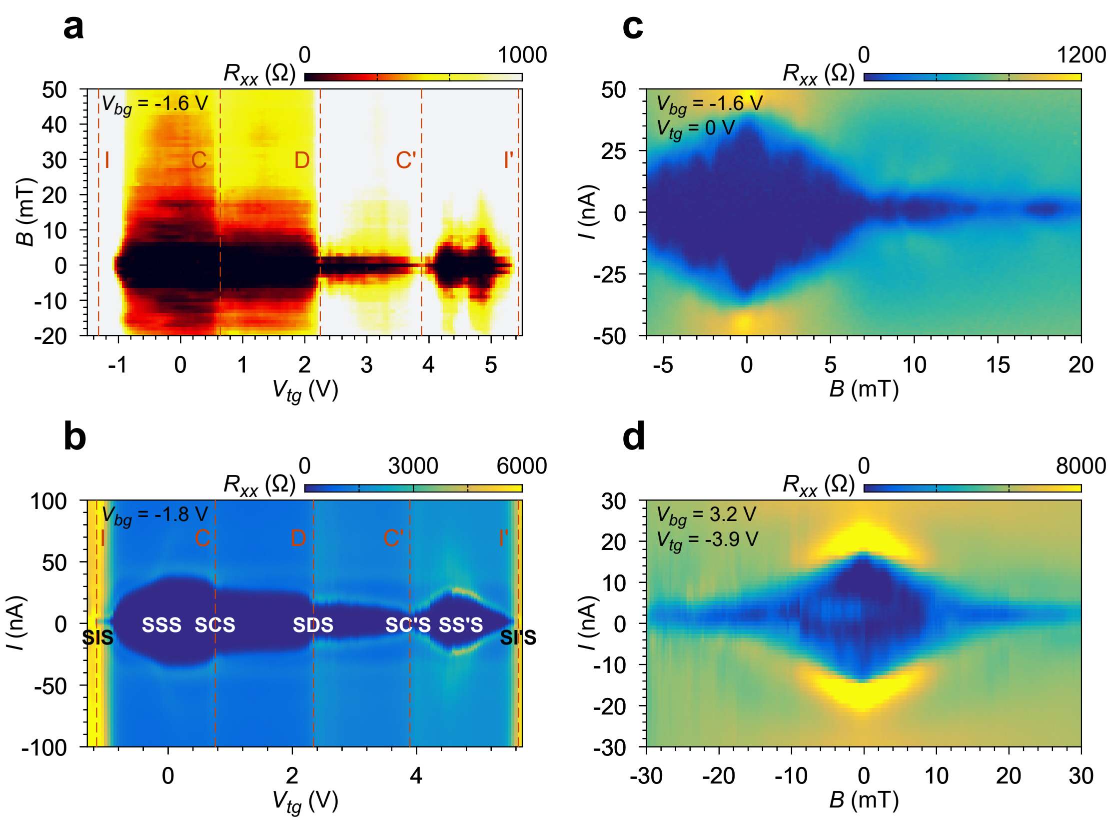

Figure S3. **Supplementary Fraunhofer patterns for device A**. (a) Magnetic field dependence of a horizontal linecut in Fig. 1c of the main text. The back gate is fixed at $V_{bg} = -1.6\,\mathrm{V}$, corresponding to the back gated region in the superconducting state. The states I, S, C, S', I' and D are labeled (see main text for definitions). (b) Resistance as a function of current bias and top gate voltage, for $V_{bg} = -1.8\,\mathrm{V}$ in the superconducting state. The barrier strength of the junction is continuously tuned by the top gate voltage. Figure reproduced from Fig. 1e of the main text. (c) Interference pattern of the junction when the narrow top gated region is in the S state and the rest of the device in the superconducting state (SSS configuration), corresponding to $V_{tg} = 0\,\mathrm{V}$. (d) A similar experiment can be realized for the device in the superconducting state in the electron side, in an S'SS' junction.

Here, we show additional Josephson effect measurements, specifically in the SSS and S'SS' regimes, in addition to the ones shown in the main text. In particular, in principle if we switch the top gate voltage to $0\,\mathrm{V}$, the entire device becomes superconducting. In this SSS case (see Fig. S3c), we do not observe a clear Fraunhofer-like pattern. The small oscillations in the critical current may arise from inhomogeneity in the device. It is also possible to realize a junction with the superconducting electrodes on the electron doping (S') by putting $V_{bg} = 3.2\,\mathrm{V}$, and use the top gate to bring the narrow region into S state, *i.e.* an S'SS' junction (similar to main text Fig. 3d, but swapping the S and S' states). Measurement in this regime is shown in Fig. S3d.

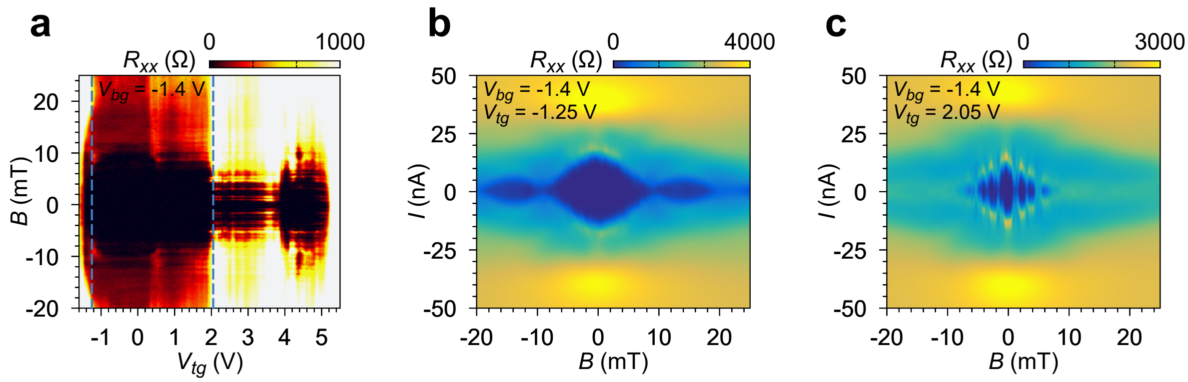

Figure S4. **Anomalous Fraunhofer pattern in device A** (a) Magnetic field dependence of a horizontal linecut in Fig. 1c of the main text with the back gate fixed at $V_{bg} = -1.4\,\mathrm{V}$. (b) Interference pattern showing a periodicity $\sim$10 mT ($\gg$ 1.5 mT reported in the other interference patterns), resembling the Fraunhofer pattern of classical bulk Josephson junctions. We attribute this anomalously large periodicity to disorder at that particular voltages, and the close proximity of this scan to the insulating state as seen in panel (a). (c) Interference pattern at the same back gate voltage, and with a top gated region close to the Dirac point, displaying a periodicity of a few mT.

We note that no in-gap features, such as multiple Andreev reflections in the SNS regime (which would appear as local minima within the superconducting gap in dV_{bias}/dI versus V_{bias} at fractions of the superconducting gap 2Δ [8]) have been observed in our samples. This might be due to the fact the gap is small compared to the spectral resolution of our measurement.

IV. ANOMALOUS PATTERN IN DEVICE A

We have argued in the main text that the oscillation period goes as $\sim \Phi_0/w^2$ for Josephson junctions in ultrathin films. However, we find that at one particular top and back gate voltage, the periodicity is anomalously larger than the above value by $\sim$6 times. This may be attributed to an inhomogeneous distribution of current across the junction due to twist angle disorder, so that the effective junction width is much smaller than the width of the sample. Fig. S4b shows the R_{xx} data at this gate configuration.

For comparison, we also include a Fraunhofer pattern with the same back gate voltage but a different top gate voltage (close to the charge neutrality point), displaying an interference pattern with a similar oscillation period compared with the ones in Fig. 3a-c of the main text.

V. TRANSPORT CHARACTERIZATION OF DEVICE B

Device B shows a similar Josephson effect as device A, despite the different device structure (shown in Fig. 4a of the main text). Fig. S5a shows the 4-probe R_{xx} resistance as a function of V_{bg} and V_{tg} (the two top gates are connected together). The $V_{tg} - V_{bg}$ map for device B is fundamentally different compared the one for device A (see Fig. 1c of the main text). The top gate of device B covers most of the device except a narrow region of a few tens of nm at the center of the device (designed to be $\sim$135 nm), in contrast to device A where the top gate only covers a narrow region at the center of the device. The horizontal features correspond to the sole effect of the back gate in the gapped region between the two top gates. Tilted features with a negative slope are associated with a constant density in the dual gated regions. The dark region indicates the superconducting phase. It corresponds to a density range spanning around the half-filling state for holes, $n = -n_s/2 \pm \delta$ (following the notation of Cao et. al. [9]).

Figure S5b displays the R-T curve in the superconducting state of device B, which shows a transition at 0.55 K, as estimated from 50% of the normal-state resistance value. Fitting the data to the Halperin-Nelson formula $R \propto \exp[-b/(T - T_{\mathrm{BKT}})^{1/2}]$, we extract $T_{BKT} = 0.3\,\mathrm{K}$ [10]. The I-V curves are shown in Fig. S5c, for $V_{tg} = -2.7\,\mathrm{V}$, $V_{bg} = -2.18\,\mathrm{V}$. The critical current is $\sim$20 nA.

Figure S5d shows the Fraunhofer pattern measured in device B in the SCS regime. The periodicity is approximately 3 mT, consistent with the estimate from theory of ultrathin Josephson junctions [11] ($w \approx 1.1\,\mu\mathrm{m}$ in device B, the expected periodicity is around $1.8\Phi_0/w^2 \approx 3\,\mathrm{mT}$). Noticeably, the tunability of the barrier strength of the weak link in the configuration with two top gates is intrinsically much weaker than for the narrow top gate configuration, due to the edge capacitance effects from the top gates. We attribute this effect to the cross-doping of the weak link caused by the stray field from the top gates (even though the top gates are not placed directly above the weak link). We note that in this device, we did not find any double periodicity as observed in device A. In addition, the field dependence of the critical currents do not reach zero, which we attribute to the nonuniform Josephson coupling across the interface [12].

Similar to Fig. 3f in the main text for device A, in Fig. S5e we show the resistance as a function of temperature and magnetic field for device B, for the same configuration as in Fig. S5d. Consistent with device A, the oscillation period is invariant with temperature, which is consistent with the nonlocal electrostatic regime governing our samples [13].

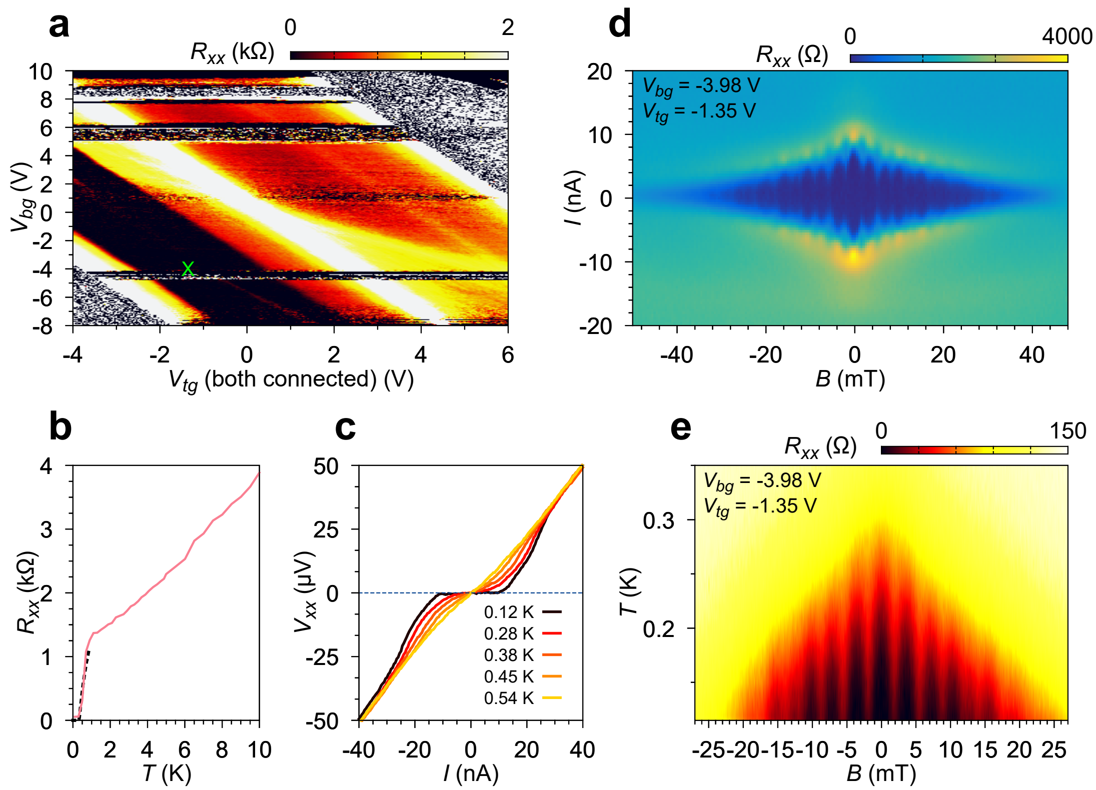

Figure S5. **Transport characterization of device B.** (a) Resistance as a function of top gates (both connected in parallel) and back gate. (b) Resistance vs. temperature trace. Device B shows a $T_c \sim 0.55\,\mathrm{K}$ ($V_{tg,both} = -2.58\,\mathrm{V}, V_{bg} = -2.4\,\mathrm{V}$). Black dotted lines show the fit to Halperin-Nelson formula $R \propto \exp[-b/(T - T_{\mathrm{BKT}})^{1/2}]$, giving $T_{BKT} = 0.3\,\mathrm{K}$ [10]. (c) Current–voltage (V_{xx}–I) curves in the superconducting region ($V_{bg} = -2.18\,\mathrm{V}$, $V_{tg,both} = -2.7\,\mathrm{V}$). (d) Characteristic interference pattern of device B for a region close to the SCS configuration, taken at the position of the green cross in panel (a). (e) Resistance as a function of magnetic field and temperature of the junction close to the SCS regime, for the same densities as the interference pattern shown in panel (d) ($V_{tg} = -1.35\,\mathrm{V}$, $V_{bg} = -3.98\,\mathrm{V}$).

VI. EVIDENCE OF SUPERCONDUCTING GAP AND SINGLE-ELECTRON TRANSISTOR BEHAVIOR IN DEVICE A

Fig. S6 shows the possible coexistence of single-electron transistor (SET) behavior and superconducting tunneling in device A. At low bias voltages, we find Coulomb diamonds, while at larger bias voltages we find features consistent with tunneling spectra into the superconducting gap. We attribute this unusual coexistence to the relatively low tunneling resistance of the insulating barriers $R \lesssim h/e^2$.

For small drain-source voltage biases, device A can be brought close to an SET regime by setting the back gate electrode to a density beyond the superlattice density for holes, and then tuning the top gate such that the central 'island' is in a superconducting state near $n = -n_s/2$. Because of the continuity of the charge density, two insulating regions in the superlattice gap $n = -n_s$ appear and provide a tunneling barrier connecting the electrodes to the central 'island' (in a similar fashion as in Fig. 5 of the main text), thus creating a junction of the form nISIn.

Figure S6a shows the four-probe differential resistance as a function of the top gate voltage for a fixed back gate and bias voltage ($V_{bg} = -4\,\mathrm{V}$, $V_{bias,applied} = 40\,\mu\mathrm{V}$). We perform the Fourier transform of these oscillations (see inset Fig. S6a) and find a prominent peak at a frequency of around $600\,\mathrm{V}^{-1}$, corresponding to a periodicity of $1/600 = 1.7\,\mathrm{mV}$. If we sweep the bias voltage between the electrodes, we indeed observe Coulomb diamonds with periodicity $\sim$1.7 mV (Fig. S6b). We note that the quality of the diamonds are not as good as in device A, which might be due to the low resistance of the insulating barriers.

On the other hand, at higher biases we find the tunneling spectra to be qualitatively similar to the edge tunneling spectra we found in devices B and C. In device A, we cannot achieve an NIS configuration since the left and right parts of the junction cannot be independently controlled (see Fig. 1a of main text for a scheme of device A). However, in the same nISIn configuration as the SET regime above ($V_{tg} = 2.8\,\mathrm{V}$, $V_{bg} = -4.5\,\mathrm{V}$), we find two prominent coherent peaks at higher bias voltages. The behavior of the tunneling spectra of device A as a function of temperature and magnetic field (Fig. S6c-d) are similar to the ones reported in the main text for devices B and C. The tunneling peaks are progressively suppressed when the temperature is increased, and become almost flat above 1.5 K. However, quantitative analysis of the gap size is unreliable since the alignment of the chemical potential of the N, S, and N regions is unknown. In a perpendicular magnetic field, the coherence peaks are suppressed, while the zero-bias anomaly persists, as discussed in the main text for devices B and C.

VII. SET OSCILLATION FREQUENCY

We note that the periodicity reported in Fig. 5d,e and the periodicity of the Coulomb diamonds in Fig. 5f ($\sim$4 mV) of the main text are not equal. While none of the qualitative observations we have made are affected, quantitatively, we attribute such a mismatch to the influence of the top gates in the central 'island' of the SET (meaning that the two top gates have significant coupling to the 'island'). In particular, Fig. 5d is taken by sweeping the back gate and correcting the top gate voltage on the right and left parts of the device to keep the densities constant, while Fig. 5f

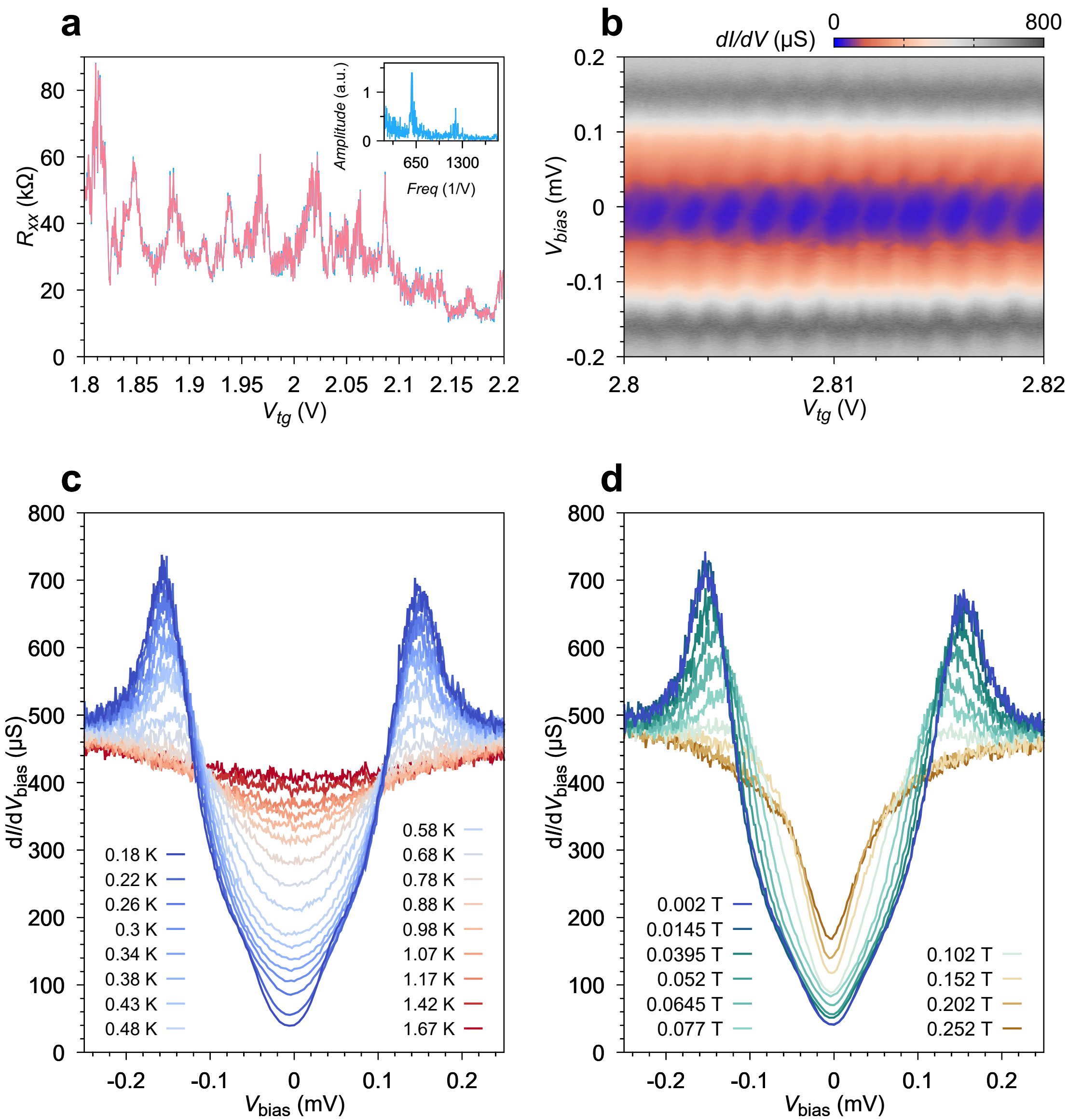

Figure S6. **Evidence of superconducting gap and single-electron transistor behavior in device A.** (a) Differential conductance as a function of top gate voltage, for two different R_{xx} pairs of contacts in blue and red ($V_{tg} \sim 2\,\mathrm{V}$, $V_{bg} = -4\,\mathrm{V}$). The signal is periodic across most of the range, with frequency $f \approx 600\,\mathrm{V}^{-1}$. The inset shows the Fourier transform of the previous signal, for the region $1.9544\,\mathrm{V} < V_{tg} < 2.09\,\mathrm{V}$ (region selected from the local Fourier transform to display the sharpest peak for easy read-out of the frequency, without loss of generality). (b) Coulomb diamonds at small V_{bias} ($V_{bg} = -4.5\,\mathrm{V}$). (c) Differential resistance as a function of bias voltage and temperature ($V_{tg} = 2.8\,\mathrm{V}$, $V_{bg} = -4.5\,\mathrm{V}$). (d) Differential resistance as a function of bias voltage and perpendicular magnetic field ($V_{tg} = 2.8\,\mathrm{V}$, $V_{bg} = -4.5\,\mathrm{V}$).

has been obtained with fixed top gates (over a much narrower range of back gate voltages than Fig. 5d). To avoid possible confusion, we have labeled the x-axis of Fig. 5f of the main text with a tilde, where the top gates are compensating at each point for the back gate voltage to keep the density constant in the left and right parts of the device.

With one electron per period, one expects the periodicity in the back gate voltage to be given by $\Delta V_{bg} = e/C_{bg}$, with e the elementary charge and C_{bg} the back gate capacitance. One can approximate, in a first approach, $C_{bg} \approx \dfrac{\epsilon_r \epsilon_0 w L}{d}$, with $\epsilon_r \approx 2.7$ (found to be the value that best fits from our Landau fans), $w \approx 0.9\,\mu$m (total width of device at the constriction), $L \approx 135\,$nm (width of the 'island' as designed by electron beam lithography, corresponding to the gap between the two top gates), and $d \approx 55\,$nm (hBN thickness). Using these values, we obtain $\Delta V_{bg} \approx 3\,$mV, which matches relatively well with the value extracted from the Coulomb blockade diamonds ($\approx 4\,$mV), given that the exact geometry of the "island" is not known a priori.

Our observations can be faithfully simulated (Fig. 5g of the main text) with an ideal single-electron transistor with capacitances $C_g = 40\,$aF, $C_1 = 110\,$aF, $C_\Sigma = 310\,$aF, where C_g is the gate capacitance, $C_\Sigma = C_1 + C_2 + C_g + C_0$, C_0 is the stray capacitance, and C_1, C_2 are the drain and source capacitances [14]. Such values are in qualitative agreement with electrostatic simulations of capacitors with similar geometry. The displayed lines correspond to the discrete energy levels at the island being aligned with one of the chemical potentials of the electrodes. For a given discrete energy level at the constriction, the range of back gate voltages for which the current can flow increases linearly with increasing bias voltage [15], resulting in the characteristic Coulomb diamonds. Their slope is associated with the capacitances (negative slope $= -0.35 = -C_g/C_1$, positive slope $= 0.2 = C_g/(C_\Sigma - C_1)$, and the x-axis separation between two consecutive diamonds is $\Delta V_{\mathrm{bias}} = 4\,\mathrm{mV} = e/C_g$). In the extreme case where $C_0 = 0$, we get $C_2 = 160\,$aF, $C_1 = 110\,$aF. In the symmetric case where $C_2 = C_1 = 110\,$aF, we get $C_0 = 50\,$aF. Within the diamonds shaded in blue (and corresponding to the situation in Fig. 5c of the main text), no electron can tunnel through the island between the electrodes.

VIII. TRANSPORT CHARACTERIZATION OF DEVICE C

Figure S7 shows the characterization of device C. The device structure of this sample is similar to that of device B (see Fig. 4a of the main text), with a 120 nm gap between the top gates. All features reported in the manuscript are qualitatively reproduced in this device. The R-T curve is shown in Fig. S7k, with a superconducting transition around $T_c \sim 0.4\,$K as extracted from 50% of the normal-state resistance value, and $T_{BKT} = 0.19\,\mathrm{K}$. The Fraunhofer patterns have a periodicity of $\sim$3 mT. The envelope of the oscillaton has a substantially different morphology than for devices A and B, which we attribute to a different microscopic current distribution. The measurement of Coulomb diamonds in the SET regime shows a nonuniform periodicity, which might be explained by the presence of two quantum dots due to inhomogeneity in the sample [15, 16].

IX. SIMULATION OF BULK AND PLANAR JOSEPHSON JUNCTIONS IN THE PRESENCE OF AN EXTERNAL MAGNETIC FIELD

We simulate the behavior of magnetic fields inside bulk and a 2D Josephson Junctions [11, 17–19], placed in an external magnetic field $\mathbf{B} = B_0\hat{z}$, to evaluate the field dependence of the maximum supercurrent both in bulk junctions and in planar 2D edge-type Josephson Junctions, given the geometry of our device A (simulation performed using $w = 1.5\,\mu\mathrm{m}$ (width of junction in y), and $L = 2.15\,\mu\mathrm{m}$ (half-length in x)). For a bulk superconductor, the magnetic field B_z satisfies the screened Poisson equation $\nabla^2 B_z - \dfrac{1}{\lambda^2}B_z = 0$ where λ is the penetration depth. The solution in a general case is an exponential decay with characteristic scale λ, and therefore in a bulk JJ the magnetic flux only penetrates in a region within 2λ centered around the junction. On the other hand, the characteristic length in a 2D superconductor is the Pearl length $\Lambda = 2\lambda^2/d$, where d is the film thickness. In a perpendicular magnetic field, the thin slab is no longer capable of expelling the magnetic field at the center and the magnetic field will penetrate the sample almost uniformly through vortices. In particular, when the length scales are much smaller than the Pearl length, $w, L \ll \dfrac{\lambda^2}{d}$, the second term of the equation can be dropped and the Poisson equation dominates the magnetic field distribution in ultrathin films $\nabla^2 B_z = 0$ [17].

In our simulation, we numerically solve for the z direction magnetic field $H(x, y)$ in the two extreme cases of an infinitely thick bulk junction and an ultrathin junction. H satisfies $\nabla^2 H - \frac{1}{\lambda^2}H = 0$ in the bulk case and $\nabla^2 H = 0$ in the 2D case. At the upper and lower boundaries $y = \pm W/2$ and at the junction $x = 0$, we set Dirichlet boundary conditions $H = H_0$ (H_0 is the externally applied field). On the left and right boundaries $x = \pm L$, we set Neumann boundary conditions $\partial_x H = 0$. In the bulk case, we use a penetration depth of $\lambda = 100\,\mathrm{nm}$. In Fig. 2c and 2d of the main text, we show the result of the simulation of the magnetic field distribution for a Josephson Junction with the junction at $x = 0$. The color scale represents the relative amplitude of $B_z = \mu_0 H_z$ inside the superconducting electrodes, i.e., the amount of magnetic field penetrating the sample. The solution is of the form $B_z \sim e^{-y/\lambda}$ with an exponential dropping of the field for the

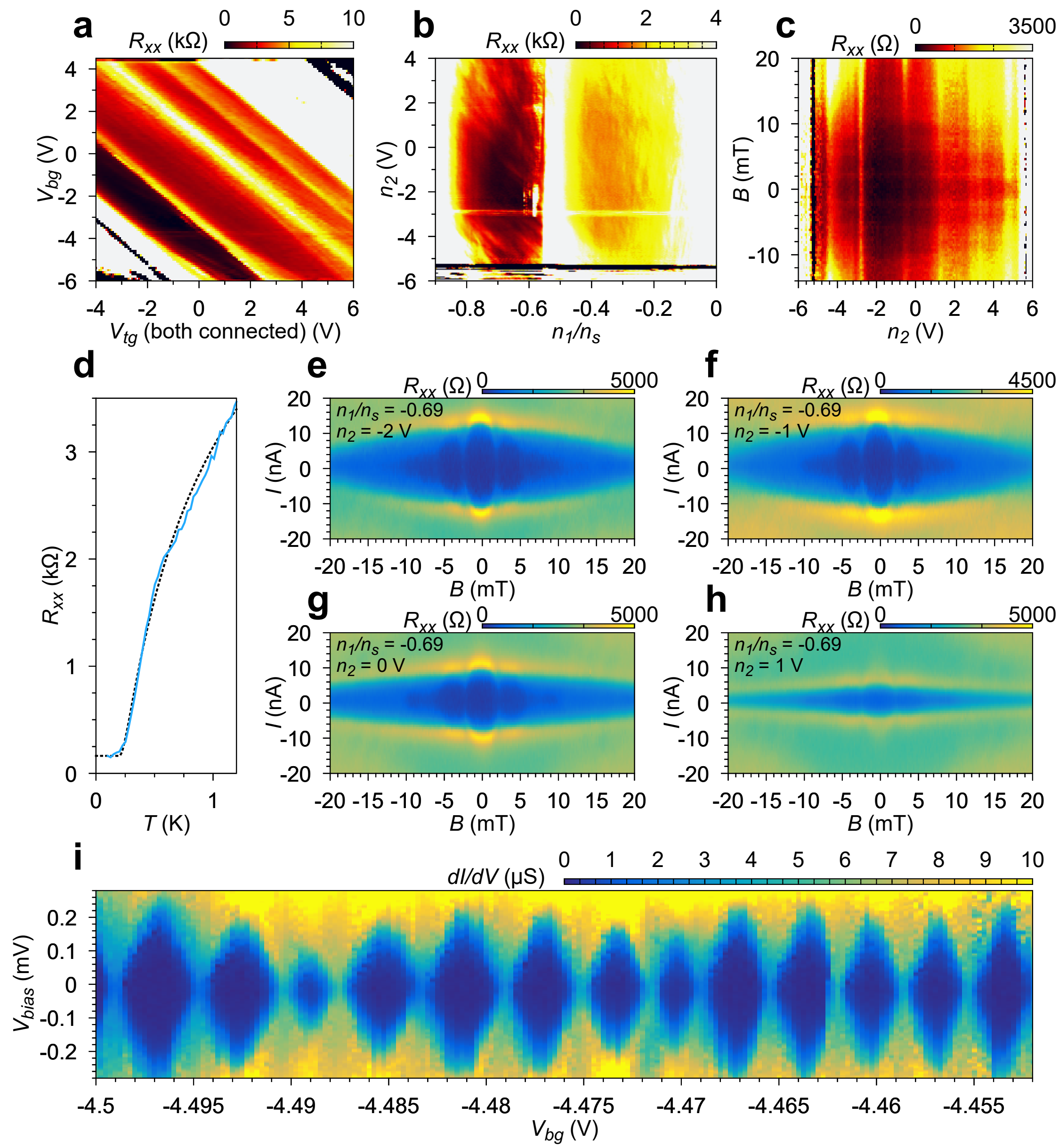

Figure S7. **Characterization of device C.** (a) V_{tg}-V_{bg} map of the resistance. The two top gates are connected together. (b) Zoom-in and rotated scan of the lower quadrant under the negative diagonal of the previous map. The x-axis denotes the density of the top gated parts (in units of the filling factor n/n_s), and the vertical axis is directly related to the back gate (with a shift to account for intrinsic doping), therefore proportional to the density in the narrow central region (transformation given by $V_{tg,left} = 8n_1/n_s - n_2 + 1.8$, $V_{tg,right} = 8n_3/n_s - n_2 + 1.8$ $V_{bg} = n_2 - 0.9$; note here both top gates are connected together and thus $n_1/n_s = n_3/n_s$). (c) n_2 vs B sweep at optimal doping $n_1/n_s = -0.69$. The periodicity as a function of the magnetic field is constant throughout n_2, as also shown in several interference patterns in Fig. (e)-(h). (d) R vs T curve for $n_2 = -0.8\,\mathrm{V}$ and $n_1/n_s = -0.699$. Black dotted lines show the fit to Halperin-Nelson formula $R \propto \exp[-b/(T - T_{\mathrm{BKT}})^{1/2}]$, giving $T_{BKT} = 0.19\,\mathrm{K}$ [10]. (i) Coulomb diamonds for device C ($V_{tg,both} = -4.8V$). The alternation of diamonds of different sizes could be an indication of two quantum dots in parallel.

bulk Josephson junction. On the other hand, for the 2D superconductor, the solution is essentially uniform, which indicates that the magnetic field is not screened by the 2D superconductor. From the Maxwell equation, current density is $\boldsymbol{j} = \nabla \times \boldsymbol{H}$, which translates to $(j_x, j_y) = (\partial_y H_z, -\partial_x H_z)$. Therefore, the contour lines of H_z are parallel to the screening current flow. Once again we see that in the bulk sample the screening currents are mostly confined at a distance λ from the edges, whereas they spread across most of the sample in the ultrathin case.

This discrepancy in magnetic field screening has an important impact on the Josephson relationship of the junction. In a wide junction, the total critical current can be computed by integrating $I_c = \int_{-w/2}^{w/2} i_c(y) \cos\gamma(y) dy$, where $i_c(y)$ is the Josephson current density and $\gamma(y)$ is the phase difference across the junction. For the bulk case, the phase $\gamma(y)$ winds as $\gamma(y) = \gamma_0 + \dfrac{2\pi}{\phi_0} 2B\lambda \cdot y$ (we assume the length of the junction in x is negligible), which gives the well-known Fraunhofer pattern with a periodicity $\Delta B = \dfrac{\phi_0}{2w\lambda}$. These formulae reflect that the magnetic field penetrates only in a distance of 2λ near the junction. For the 2D case, on the other hand, since the magnetic field is no longer localized at the junction, in general the phase difference $\gamma(y)$ cannot be analytically written down. Instead, we obtain $\gamma(y)$ by numerically integrating the relationship $\partial_y \gamma(y) = -\frac{4\pi\mu_0\lambda^2}{\phi_0} j_y(0^+, y)$ (take $\lambda \to \infty$ in 2D limit) [17]. The periodicity ΔB is no longer constant in this case, but can be approximated at larger fields as $\Delta B' \sim \dfrac{1.8\phi_0}{w^2}$ [11, 20].

X. SIMULATION OF THE CHARGE DISTRIBUTION AND THE APPEARANCE OF INSULATING BARRIERS FOR THE TUNNELING AND THE SINGLE-ELECTRON TRANSISTOR

At the magic angle, the band structure of TBG exhibits bandgaps on the order of ∼30 meV at densities $n = \pm n_s$ [4]. In this work, we exploit these superlattice gaps as in-situ tunneling barriers for tunneling spectroscopy of the superconducting gap and the single-electron transistor.

In the case of the tunneling spectroscopy configuration, as shown in Fig. 4 of the main text, one side of the sample is set to a density larger than the superlattice gap, and the other side to a density lower than the superlattice gap. Therefore we expect to have at least one point in space at which the density equals the superlattice density and thus is insulating. If quantum capacitance effects are taken into account, the density will in fact have a plateau at the superlattice density. In order to simulate this phenomenon, we self-consistently solve the electrostatic model governed by a Poisson equation with a nonlinear boundary condition. In the dielectric, electrostatic potential satisfies $\nabla^2 V = 0$. The boundary conditions are taken to be $V = V_{g1}$ at the left top gate, $V = V_{g2}$

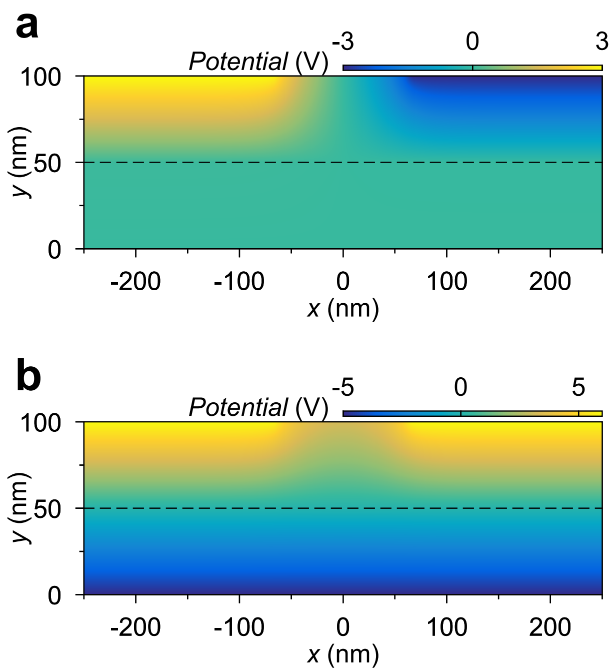

Figure S8. **Simulation of the potential for the Tunneling (a) and SET (b) configurations.** Two top gates are added at y=100 nm for positive and negative x axis, and a back gate at y=0, setting the boundary conditions V_{g1}, V_{g2} and V_{g0} (see main text). The dashed line at $y = 50\,\mathrm{nm}$ denotes the MATBG.

at the right top gate, $V = V_{g0}$ at the back gate. Side boundaries are set to Neumann conditions $\partial_x V = 0$.

Since the MATBG is grounded, it has zero *electrochemical* potential at any point on it $\mu(n(x)) - V(x) = 0$, where $n(x) = [E_y^+(x) - E_y^-(x)]/e$ is the electron charge density, and $\mu(n)$ is the chemical potential of MATBG. The boundary condition at the MATBG is therefore $V_{\mathrm{TBG}}(x) = \mu\left(\frac{1}{e}(\partial_y V^+ - \partial_y V^-)\right)$ [21]. Here, $E^\pm$ and $V^\pm$ are the electric field and electric potential above and below TBG respectively. To capture the fundamental features with minimal complexity, we assume a band gap of 30 meV and parabolic bands with effective masses $m_1 = 0.4 m_e$ for $n > -n_s$ and $m_2 = 0.05 m_e$ for $n < -n_s$. The problem is solved with an iterative method. In each iteration, V^n_{TBG} is calculated from $V^n_{\mathrm{TBG}} = \mu\left(\frac{1}{e}(\partial_y V^{n-1,+} - \partial_y V^{n-1,-})\right)$, and the Poisson equation $\nabla^2 V = 0$ is solved using boundary condition V^n_{TBG} to obtain V^n.

For the tunneling spectroscopy configuration (displayed in Fig. 4 of the main text), we use the values $V_{g1} = 3\,\mathrm{V}$, $V_{g2} = -3\,\mathrm{V}$, and $V_{g0} = 0\,\mathrm{V}$ (see Fig. S8a). This results in the density induced in the twisted bilayer graphene displayed in Fig. 4b of the main text, and a barrier width on the order of 10 nm. An analogous procedure is performed for the SET configuration (Fig. S8b) with $V_{g1} = 6\,\mathrm{V}$, $V_{g2} = 6\,\mathrm{V}$, and $V_{g0} = -5\,\mathrm{V}$. The resulting density is displayed in Fig 5a of the main text.

XI. FURTHER ANALYSIS OF THE TUNNELING SPECTRA IN DEVICES B AND C

Fig. S9 shows the tunneling spectra for device C at a fixed back gate ($V_{bg} = -1.2\,\mathrm{V}$) and fixed top right gate voltage ($V_{tg,right} = -7.5\,\mathrm{V}$), while varying the top left gate voltage. In this configuration, we observe tunneling from a region in the normal state with density $n_3/n_s \approx -1.2n_s$ into different regions on the left side of the device (I, S, C, metallic region with hole doping in between D and C, D, and C'), via the insulating barrier I (in a similar fashion as shown in Fig 4b of the main text). Spectra are plotted for zero magnetic field (solid lines) and in a perpendicular magnetic field of $0.2\,\mathrm{T}$ (dashed lines). Tunneling peaks fitting the phenomenology of superconducting coherence peaks (represented in black, with a thicker trace) are only observed at densities near the superconducting state ($V_{tg,left} = -4.1\,\mathrm{V}$, corresponding to the configuration SIn where the left part of the device is at a density $n_1/n_s \approx -0.775n_s$). The coherence peaks disappear in the presence of a perpendicular magnetic field (denoted by the double-headed arrows in Fig. S9), as explained in the main text.

For both devices B and C, four different pieces of evidence support the conclusion that the tunneling spectra shown in Fig. 4 indeed correspond to the superconducting gap of MATBG. First, the 4-terminal transport obtained at the same densities display zero or close to zero resistance. Second, the shape of the coherence peaks surrounding the spectroscopic gap fits well to our model for the superconducting quasiparticle density of states. Third, the coherence peaks disappear with temperature in the appropriate range. Finally, the coherence peaks disappear in a magnetic field (although there is an unrelated conductance minimum surviving at much higher fields, as explained in the main text, attributed to a separate mechanism). We also reiterate, from Fig. S9, that the only densities at which coherence peaks are observed coincide with densities at which the superconducting state is observed in transport.

XII. FITS TO THE TUNNELING DATA

Theoretical fits to the tunneling data shown in Fig. 4 of the main text were performed using a simple model for the tunneling conductance between a metal and a superconductor [22]. This model involves the product of the quasiparticle density of states in the superconductor and a constant

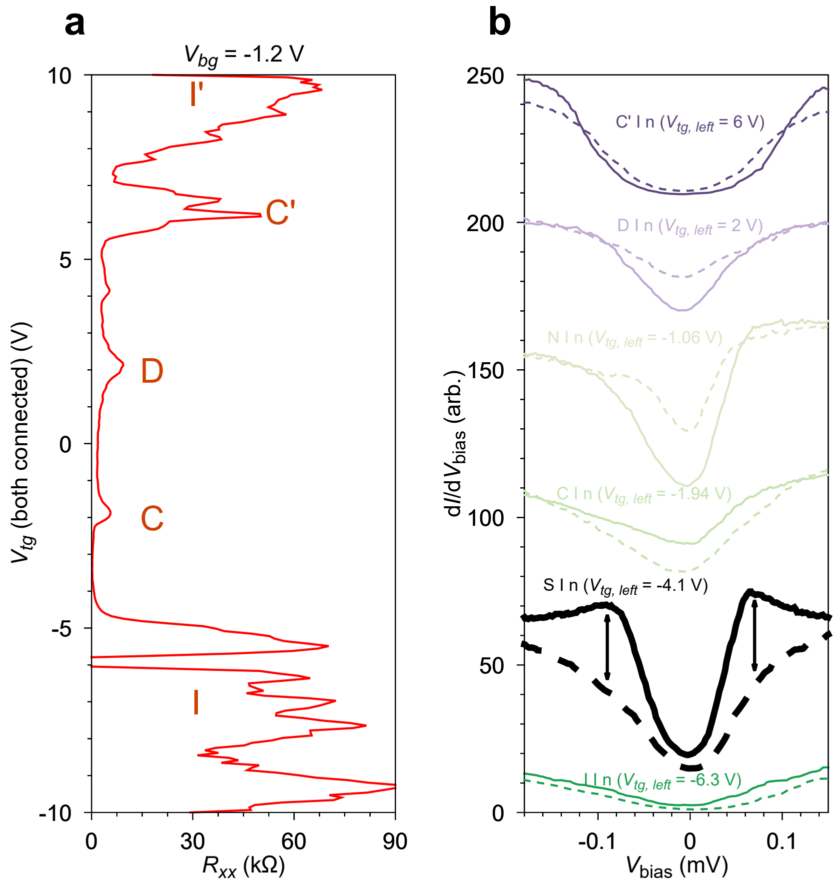

Figure S9. **Tunneling spectra across the different states in MATBG.** (a) Linecut in the back gate-top gate map for device C at $V_{bg} = -1.2\,\mathrm{V}$. Labels in red denote features induced by the top gate gates, following the convention of the main text. (b) Tunneling spectra for device C. The back gate ($V_{bg} = -1.2\,\mathrm{V}$) and top right gate ($V_{tg,right} = -7.5\,\mathrm{V}$) voltages are fixed, and the top left gate voltage is varied. This allows tunneling from the right region in the normal state n with density $n_3/n_s \approx -1.2n_s$ into different regions on the left side of the device (I, S, C, N, D, and C'), via the insulating barrier I. Spectra are shown in zero magnetic field (solid lines) and in a perpendicular magnetic field of 0.2 T (dashed traces).

density of states with the derivative of the Fermi occupation function,

$$\frac{dI}{dV} \propto \int_{-\infty}^{\infty} dE\, N_s(E) \frac{df}{dV}, \tag{1}$$

for $f(E) = \left[\exp\left(\frac{E-eV}{k_BT}\right)+1\right]^{-1}$ at temperature T and bias voltage $V = V_{\text{bias}}$ (the constant density of states in the normal metal is a constant prefactor and is ignored here). The quasiparticle density of states at zero temperature is given by [23],

$$N_s(E) = N_0 \,\mathrm{Re}\, \frac{E}{\sqrt{E^2 - \Delta_{\mathbf{k}}^2}}, \tag{2}$$

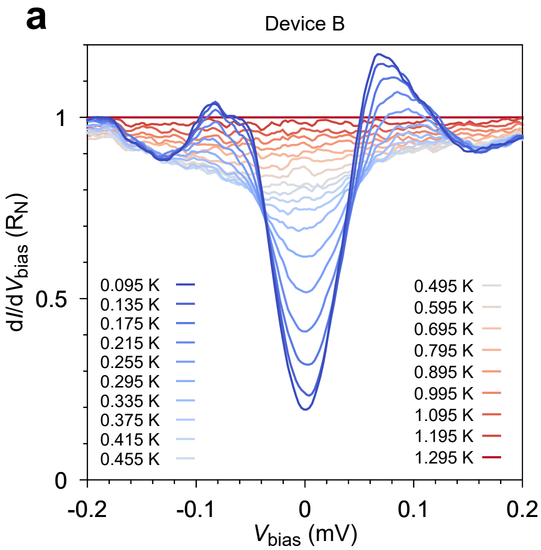

Figure S10. **Normalized spectra of the superconducting gap in MATBG from Fig. 4 of the main text.** (a) Normalized tunneling spectra with respect to the spectrum at 1.295 K as a function of temperature for device B. (b) Similarly, normalized tunneling spectra with respect to the spectrum at 1 K as a function of temperature for device C.

with $\Delta_{\mathbf{k}} = \Delta$ for an isotropic (s-wave) gap Δ, and with the substitution $E \to E + i\Gamma$ incorporating a phenomenological quasiparticle lifetime broadening, Γ (Dynes broadening). At temperatures well above the superconducting transition, the tunneling spectra in devices B and C exhibit background curvature attributable to details of the normal metal density of states and the tunneling barrier. To isolate the superconducting part of the tunneling data, we perform a background correction before fitting the data to Eq. 1. This is carried out by first fitting a polynomial function, $(dI/dV)_{\mathrm{poly}}$, to a tunneling spectrum acquired at a sufficiently high temperature for each device (where the changes in spectroscopic behavior begin to saturate with increasing temperature), and then dividing away this smooth background function $(dI/dV)_{\mathrm{sub}} = (dI/dV)_{\mathrm{raw}}/(dI/dV)_{\mathrm{poly}}$ such that the background-corrected data $(dI/dV)_{\mathrm{sub}}$ do not contain the curvature observed at high temperatures (see Fig. S11a). The differential conductance in Eq. 1 is then fit to the background-corrected tunneling data taken at the lowest temperature with Δ and Γ as free parameters, along with T, to account for a potentially elevated electron temperature, and an overall scale factor. The data shown in the main text are raw data, without any background correction. To show the correspondence between the fits to the superconducting (SC) part of tunneling spectrum and the raw data, we include the polynomial background in the plotted fits by multiplying each fit by the polynomial part

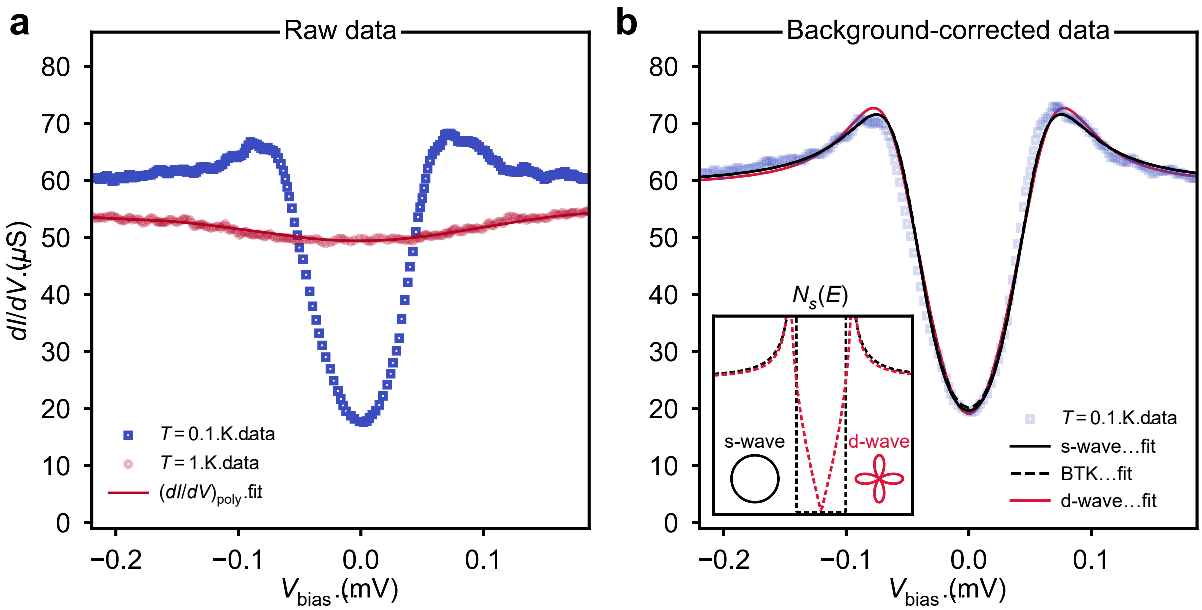

Figure S11. **Fitting procedure for tunneling data from device C** (a) Raw tunneling data and (b) background-corrected data with s-wave and BTK fits superimposed. Best-fit parameters are $\Delta = 51\,\mu\text{eV}$, $T = 113\,\text{mK}$, and $\Gamma = 14\,\mu\text{eV}$ in both cases, with all values of $Z \geq 1.1$ fitting equally well in the BTK case. An anisotropic d-wave fit, using $\Delta_{\mathbf{k}} = \Delta\cos(2\theta)$, also produces a high-quality fit with amplitude $\Delta = 64\,\mu\text{eV}$, $T = 152\,\text{mK}$ and $\Gamma \approx 0$. Although the underlying quasiparticle densities of states $N_s(E)$ differ substantially (inset, shown with same axis limits as (a)-(b)), the two fits are indistinguishable at the finite temperatures of the experiment.

extracted from the data at high temperature, $(dI/dV)_{\text{fit}} = (dI/dV)_{\text{SC}} \times (dI/dV)_{\text{poly}}$. Employing a similar fitting procedure using the standard Blonder-Tinkham-Klapwijk (BTK) relation [24] (with $E \to E + i\Gamma$) rather than Eq. 2 also fits the data nicely (see BTK fit in Fig. S11b). Using the BTK formula, we find similar Δ and Γ values and a dimensionless barrier strength value $Z > 1$, indicating a low-transparency barrier between the normal metal and superconducting regions. The value $Z > 1$ supports our conclusion that the barrier region is indeed in the tunnel coupling limit, enabling our spectroscopic analysis of the superconducting gap.

Though the fits described here employ an isotropic assumption for the order parameter, we must emphasize that the quality of these fits do not preclude order parameters with other symmetries. For instance, we find that a modification of Eq. 2 using the substitution $\Delta_{\mathbf{k}} = \Delta\cos(2\theta)$ and integrating over the polar angle $N_s(E) = (1/\pi)\int d\theta N_s(E,\theta)$, a model for a nodal order parameter with $d_{x^2-y^2}$ symmetry (d-wave), fits our tunneling data equally well (Fig. S11b). An order parameter with d_{xy} symmetry ($\Delta_{\mathbf{k}} = \Delta\sin(2\theta)$) produces an identical tunneling spectrum. While both the isotropic and d-wave fits appear to match the data, note that the implied quasiparticle densities of states $N_s(E)$ differ substantially in the two cases (see inset of Fig. S11b). However, these differences are obscured in our experiment by thermal and lifetime broadening, preventing us from determining the symmetry of the underlying order parameter.

One might also wonder whether the temperature dependence of these curves could provide additional information about the symmetry of the superconducting order parameter. Although we do expect differences in both the shape of the spectrum and in the temperature dependence of the magnitude of the order parameter as a function of temperature Δ(T), there are at least three reasons that this analysis fails in practice: (1) The shape of the expected dI/dV curves at higher temperatures are nearly indistinguishable due to thermal broadening. (2) We do not have an independent measure of the electronic temperature in the MATBG, and therefore an accurate measure of (T) is not possible (e.g. to compare the shape of these curves). (3) The edge-tunneling process may include tunneling into a thin, proximitized metal region between the insulator and superconductor that produces an underestimation of the true bulk value of the gap in the superconductor. To support this, we have performed further calculations to investigate whether it would be possible to distinguish between s-wave and d-wave order parameters from the temperature dependence of the spectral curves from device C. In Figure S12, we show (a) our background corrected data, (b) a model for the temperature dependence of an s-wave spectrum including thermal broadening and (c) a similar model for a d-wave gap. The two models are based on the tunneling current expressions given in SI Eqs. (1) and (2), using the approximate formula [25],

$$\Delta(T) = \Delta(0) \tanh\left(\pi k_b T_c/\Delta(0)\sqrt{a(T/T_c - 1)}\right), \tag{3}$$

with $\Delta(0) = 51\,\mu\text{eV}$ and $T_c = 0.85\,\text{K}$ (in reasonable agreement with our transport data given the broadness of the superconducting transition and the uncertainty in the determination of the exact electronic temperature of the system) to determine the evolution of the gap with temperature, using a matching set of temperatures to those measured in the experiment. Thermal broadening is included via the Fermi occupation function in Eq. 1 and quasiparticle lifetime broadening is set to $\Gamma = 14\,\mu\text{eV}$ for the s-wave model and $\Gamma \approx 0$ for the d-wave model, as in the best fits from Fig. S11 at 100 mK. Using these parameters we find the best agreement with our experimental curves over the full temperature range and conclude that, based on this model, thermal broadening prevents distinguishing the spectral curves within the range of temperatures available in our system. Moreover, a possible mismatch between the measured temperature of our Cernox thermometer and

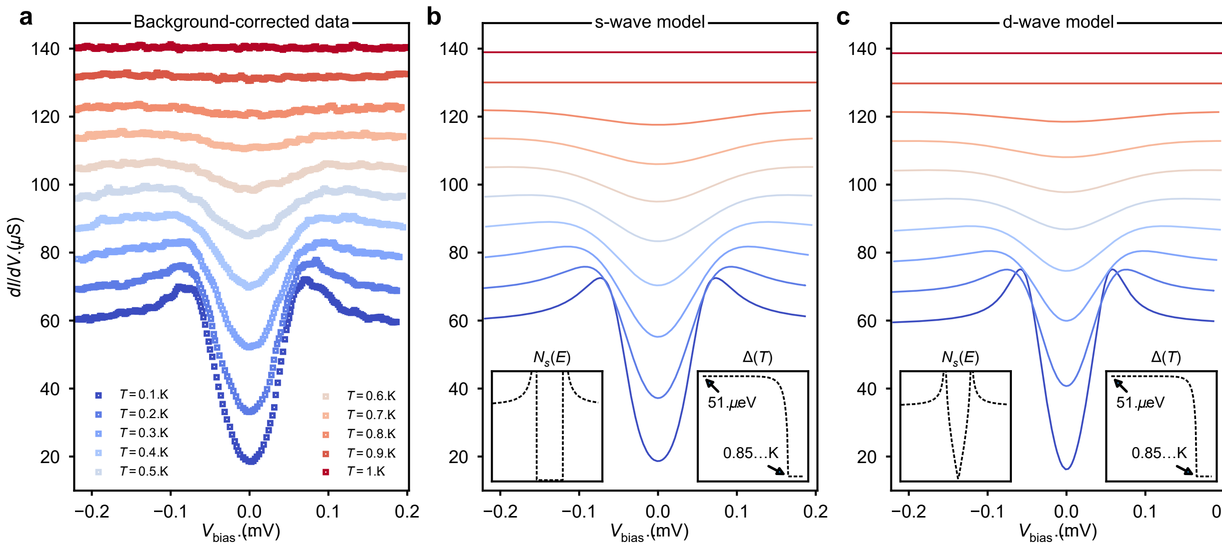

Figure S12. **Temperature evolution of the superconducting gap for device C.** (a) Background corrected data, (b) a model for the temperature dependence of an s-wave tunneling spectrum including thermal broadening and (c) a similar model for a d-wave gap. The details of the models and the background subtraction are explained in the text.

the electronic temperature in the MATBG further complicates this analysis. For instance, while the s-wave and d-wave models shown for $T = 0.1\,\mathrm{K}$ in panels (b) and (c) of Fig. S12 differ slightly, a more accurate best-fit analysis (as shown in Fig. S12) shows that the d-wave model is nearly indistinguishable from the s-wave model even if the electronic temperature is elevated only slightly (e.g. $\sim$150 mK in the best fit analysis). It would therefore be difficult to draw a conclusion distinguishing between these two superconducting (or other) order parameters based on our present measurements. Nevertheless, future spectroscopic measurements from tunneling in similar devices may uncover additional details of the superconductivity in MATBG.

---

[1] Goossens, A. M. *et al.* Mechanical cleaning of graphene. *Applied Physics Letters* **100**, 073110 (2012).

[2] Rosenberger, M. R. *et al.* Nano-“Squeegee” for the Creation of Clean 2D Material Interfaces. *ACS Applied Materials & Interfaces* **10**, 10379–10387 (2018).

[3] Wang, L. *et al.* One-Dimensional Electrical Contact to a Two-Dimensional Material. *Science* **342**, 614–617 (2013).

[4] Cao, Y. *et al.* Correlated insulator behaviour at half-filling in magic-angle graphene superlattices. *Nature* **556**, 80–84 (2018).

[5] Cao, Y. *et al.* Unconventional superconductivity in magic-angle graphene superlattices. *Nature* **556**,

43–50 (2018).

[6] Cao, Y. *et al.* Superlattice-Induced Insulating States and Valley-Protected Orbits in Twisted Bilayer Graphene. *Physical Review Letters* **117**, 116804 (2016).

[7] Hesp, N. C. H. *et al.* Collective excitations in twisted bilayer graphene close to the magic angle 36.

[8] Octavio, M., Tinkham, M., Blonder, G. E. & Klapwijk, T. M. Subharmonic energy-gap structure in superconducting constrictions. *Phys. Rev. B* **27**, 6739 (1983).

[9] Cao, Y. *et al.* Strange metal in magic-angle graphene with near planckian dissipation. *Phys. Rev. Lett.* **124**, 076801 (2020).

[10] Halperin, B. I. & Nelson, D. R. Resistive transition in superconducting films. *Journal of Low Temperature Physics* **36**, 599–616 (1979).

[11] Moshe, M., Kogan, V. G. & Mints, R. G. Edge-type Josephson junctions in narrow thin-film strips. *Physical Review B* **78**, 020510 (2008).

[12] Sinko, M. R. *et al.* Superconducting Edge Contact and Quantum Interference Between Two-Dimensional van der Waals and Three-Dimensional Conventional Superconductors. *arXiv:1911.09711 [cond-mat]* (2019). ArXiv: 1911.09711.

[13] Boris, A. A. *et al.* Evidence for Nonlocal Electrodynamics in Planar Josephson Junctions. *Physical Review Letters* **111**, 117002 (2013).

[14] Heij, C. P. *Single-charge transport in coupled nanostructures.* Ph.D. thesis, TU Delft (2001).

[15] Ihn, T. *et al.* Graphene single-electron transistors. *Materials Today* **13**, 44–50 (2010).

[16] van der Wiel, W. G. *et al.* Electron transport through double quantum dots. *Reviews of Modern Physics* **75**, 1–22 (2002).

[17] Clem, J. R. Josephson junctions in thin and narrow rectangular superconducting strips. *Physical Review B* **81**, 144515 (2010).

[18] Kogan, V. G., Dobrovitski, V. V., Clem, J. R., Mawatari, Y. & Mints, R. G. Josephson junction in a thin film. *Physical Review B* **63**, 144501 (2001).

[19] Rosenthal, P. A., Beasley, M. R., Char, K., Colclough, M. S. & Zaharchuk, G. Flux focusing effects in planar thin-film grain-boundary Josephson junctions. *Applied Physics Letters* **59**, 3482–3484 (1991).

[20] Clem, J. R. Effect of nearby Pearl vortices upon the Ic versus B characteristics of planar Josephson junctions in thin and narrow superconducting strips. *Physical Review B* **84**, 134502 (2011).

[21] Jackson, J. D. *Classical electrodynamics* (Wiley, 1975), 2nd edn.

[22] Tinkham, M. *Introduction to Superconductivity* (Dover Publications, 2004), 2nd edn.

[23] Won, H. & Maki, K. d-wave superconductor as a model of high-t_c superconductors. *Physical Review B* **49**, 1397–1402 (1994).

[24] Blonder, G. E., Tinkham, M. & Klapwijk, T. M. Transition from metallic to tunneling regimes in superconducting microconstrictions: Excess current, charge imbalance, and supercurrent conversion. *Physical Review B* **25**, 4515–4532 (1982).

[25] Gross, F. *et al.* Anomalous temperature dependence of the magnetic field penetration depth in super-

conducting UBe_{13}. *Zeitschrift für Physik B Condensed Matter* **82**, 243–255 (1991).